A semi-implicit hybrid finite volume / finite element scheme for all Mach number flows on staggered unstructured meshes

S. Busto[a,*], L. Río-Martín[a,b], M.E. Vázquez-Cendón[b], M. Dumbser[a]

[a] *Laboratory of Applied Mathematics, DICAM, University of Trento, via Mesiano 77, 38123 Trento, Italy*
[b] *Department of Applied Mathematics, University of Santiago de Compostela, 15782 Santiago de Compostela, Spain*

Abstract

In this paper a new hybrid semi-implicit finite volume / finite element (FV/FE) scheme is presented for the numerical solution of the compressible Euler and Navier-Stokes equations at all Mach numbers on unstructured staggered meshes in two and three space dimensions. The chosen grid arrangement consists of a primal simplex mesh composed of triangles or tetrahedra, and an edge-based / face-based staggered dual mesh. The governing equations are discretized in conservation form. The nonlinear convective terms of the equations, as well as the viscous stress tensor and the heat flux, are discretized on the dual mesh at the aid of an explicit local ADER finite volume scheme, while the implicit pressure terms are discretized at the aid of a continuous $\mathbb{P}^1$ finite element method on the nodes of the primal mesh. In the zero Mach number limit, the new scheme automatically reduces to the hybrid FV/FE approach forwarded in [1] for the incompressible Navier-Stokes equations. As such, the method is asymptotically consistent with the incompressible limit of the governing equations and can therefore be applied to flows at all Mach numbers. Due to the chosen semi-implicit discretization, the CFL restriction on the time step is only based on the magnitude of the flow velocity and not on the sound speed, hence the method is computationally efficient at low Mach numbers. In the chosen discretization, the only unknown is the scalar pressure field at the new time step. Furthermore, the resulting pressure system is symmetric and positive definite and can therefore be very efficiently solved with a matrix-free conjugate gradient method.

In order to assess the capabilities of the new scheme, we show computational results for a large set of benchmark problems that range from the quasi incompressible low Mach number regime to compressible flows with shock waves.

Keywords: all Mach number flow solver, pressure-based projection method, finite element method, finite volume scheme, semi-implicit scheme on unstructured staggered meshes, ADER methodology

1. Introduction

Since their first formulation more than 200 years ago, the Euler and Navier-Stokes equations describing the flow of inviscid and viscous fluids have always been a big challenge, both from the theoretical as well as from the numerical point of view. The Euler equations can be directly derived from first principles by considering the conservation of mass, momentum, and total energy. Their extension to the Navier-Stokes equations is then achieved at the aid of appropriate assumptions for the viscous stress tensor and the heat flux. In the most general case, the fluid is assumed to be *compressible*, but different flow regimes can be identified at the aid of the dimensionless *Mach number* $M = \|\mathbf{v}\|/c$, where $\mathbf{v}$ and c are the fluid velocity and the sound speed, respectively. For $M \to 0$ the behaviour of the fluid becomes the one of an *incompressible* medium, with the well-known condition $\nabla \cdot \mathbf{v} = 0$, which states that the velocity field must

*Corresponding author
Email addresses: saray.bustoulloa@unitn.it (S. Busto), laura.delrio@unitn.it (L. Río-Martín), elena.vazquez.cendon@usc.es (M.E. Vázquez-Cendón), michael.dumbser@unitn.it (M. Dumbser)

become divergence-free when the flow becomes incompressible in the limit $M \to 0$. This asymptotic limit was rigorously studied for the first time by Klainerman and Majda in [2, 3]. The asymptotic analysis shows that in the incompressible limit and without compression from the boundary, the pressure can be decomposed into two different contributions: a spatially constant part of the pressure satisfying the equation of state and some fluctuations of the pressure around that constant, governed by the well-known *elliptic* pressure Poisson equation. This change of behaviour for $M \to 0$ is important since the original governing equations are hyperbolic-parabolic they can even exhibit shock waves for high Mach numbers. Because of this changing behaviour of the equations according to the Mach number, it is notoriously difficult to construct suitable numerical schemes which can be simultaneously applied to compressible high Mach number flows with shock waves and also to incompressible or nearly incompressible low Mach number flows.

Typically, the *incompressible* Euler and Navier-Stokes equations are solved via *semi-implicit pressure-based* schemes of the finite difference type on staggered grids, see e.g. [4, 5, 6, 7, 8, 9, 10, 11, 12], or at the aid of *continuous finite elements* [13, 14, 15, 16, 17, 18, 19]. Instead, for the simulation of *compressible* flows at higher Mach numbers and with shock waves, *explicit density-based* finite volume schemes of the Godunov-type on collocated grids are usually more popular, see [20, 21, 22, 23, 24, 25, 26, 27, 28, 29].

A first attempt to generalize semi-implicit methods to the more general case of compressible flows was made by Casulli and Greenspan in [30], but the proposed scheme was not conservative and therefore could not be used for the treatment of high Mach number flows with shock waves. Semi-implicit schemes that explicitly make use of the low Mach number asymptotics of the governing partial differential equations can be found in [31, 32, 33, 34], while the first conservative staggered semi-implicit pressure-based scheme for compressible flows was introduced by Park and Munz in [35]. The scheme [35] can be considered as one of the first *all Mach number* flow solvers ever proposed in the literature. The particular splitting of explicit convective terms and implicit pressure terms used in [35] was later studied in more detail in [36] in order to construct a novel flux-vector splitting method. Since the pioneering work of Park and Munz, the development of all Mach number flow solvers, i.e., of numerical schemes that work at the same time for high Mach number flows with shock waves and in the incompressible limit of the equations, has become a very active research field with many relevant contributions, see e.g. [37, 38, 39, 40, 41, 42, 43, 44, 45, 46] and references therein. For special low Mach number corrections to explicit density-based finite volume schemes, the reader is referred to [47, 48].

On unstructured simplex meshes, classical continuous finite element methods can nowadays be considered as standard for the numerical solution of the incompressible Navier-Stokes equations. Instead, the construction of *discontinuous* Galerkin finite element schemes for the solution of the compressible and incompressible Navier-Stokes equations on unstructured meshes is still the topic of ongoing research. For an overview of high order DG schemes for the compressible and incompressible Navier-Stokes equations, see for example [49, 50, 51, 52, 53, 54, 55, 56, 57, 58, 59, 60], but this list does not pretend to be complete. Concerning high order semi-implicit discontinuous Galerkin methods on *collocated grids* we refer to [61, 62, 63], while a new family of semi-implicit *staggered* discontinuous Galerkin schemes for the discretization of the incompressible and compressible Navier-Stokes equations was recently forwarded in [64, 65, 66, 67, 68, 69].

To round-up this brief literature review, we would also like to point the reader to a very recent and completely different approach for the solution of the Navier-Stokes equations, which consists in embedding the Navier-Stokes equations in a more general first order hyperbolic system with stiff relaxation source terms that is able to describe continuum mechanics as a whole, from nonlinear elastic solids over visco-plastic solids to Newtonian and non-Newtonian fluids, and from which for small enough relaxation times the Navier-Stokes equations are retrieved in the limit of a much more general model that contains continuum mechanics as a whole, see [70, 71, 72, 73, 74]. This universal model is based on the pioneering work of Godunov and Romenski on symmetric hyperbolic and thermodynamically compatible systems and on nonlinear hyperelasticity, see e.g. [75, 76, 77, 78, 79] and references therein. For an alternative hyperbolic relaxation approach for the discretization of the Navier-Stokes equations, the reader is referred to [80].

The numerical methods previously discussed were all of a specific type, say finite volume, finite difference, or finite element schemes. More recently in a series of papers a new class of hybrid finite volume / continuous finite element methods on *staggered* unstructured meshes in 2D and 3D has been proposed in [81, 1, 82, 83] for the solution of the incompressible Navier-Stokes equations and for the low Mach number limit of the

weakly compressible equations. In these hybrid schemes, the nonlinear convective part of the equations was solved at the aid of an explicit finite volume scheme on an edge-based staggered dual mesh, see [84, 1] for a more detailed analysis, and the pressure equation was solved with a continuous finite element method on the primal grid. The advantage of this hybrid approach is that for each part of the governing PDE system the most appropriate numerical method could be used, since it is well-known that explicit finite volume methods are more suitable for the discretization of nonlinear hyperbolic PDE systems, while the clear strength of continuous finite element methods lies in the discretization of elliptic problems.

It is therefore the aim of the present paper to provide a novel pressure-based semi-implicit hybrid finite element / finite volume method on staggered unstructured meshes that can solve the compressible Euler and Navier-Stokes equations in a wide range of Mach numbers, which is a very substantial generalization compared to the incompressible and weakly-compressible flow solvers presented in [81, 1, 83]. Following the seminal ideas outlined in [35, 36, 39], the nonlinear convective part of the equations will be discretized via an explicit finite volume scheme, while the resulting pressure equation, which is more complex than the simple pressure Poisson equation that typically results from the discretization of the incompressible Navier-Stokes equations, is discretized on the primal mesh at the aid of classical continuous finite elements. The semi-implicit discretization allows choosing a time step that is not limited by the sound speed, but only by the velocity magnitude. The new hybrid scheme of this paper is designed to work simultaneously for incompressible and low Mach number flows, as well as for compressible flows including shock waves. For $M \rightarrow 0$ the scheme reduces to the hybrid FV/FE method for the incompressible Navier-Stokes equations forwarded in [1]. As such, the proposed method is an asymptotic preserving (AP) all Mach number flow solver.

The rest of the paper is organized as follows: in Section 2 we first introduce the governing equations considered in this paper; next, in Section 3 we present their discretization via the new semi-implicit hybrid finite-volume / finite-element scheme on staggered meshes. In Section 4 we present numerical results for a wide range of Mach numbers, from almost incompressible flows to supersonic flows with shock waves. The conclusions and an outlook to further work are given in Section 5.

2. Governing partial differential equations

Let us denote by ρ the density, $\mathbf{u} = (u, v, w)$ is the velocity vector and E is the specific total energy then, the compressible Navier-Stokes equations given in conservative form read

$$\frac{\partial \rho}{\partial t} + \nabla \cdot (\rho \mathbf{u}) = 0, \tag{1}$$

$$\frac{\partial \rho \mathbf{u}}{\partial t} + \nabla \cdot (\rho \mathbf{u} \otimes \mathbf{u}) + \nabla p - \nabla \cdot \boldsymbol{\tau} = \rho \mathbf{g}, \tag{2}$$

$$\frac{\partial \rho E}{\partial t} + \nabla \cdot [\mathbf{u} (\rho E + p)] - \nabla \cdot (\boldsymbol{\tau} \mathbf{u}) + \nabla \cdot \mathbf{q} = \rho \mathbf{g} \cdot \mathbf{u}, \tag{3}$$

where $\mathbf{g}$ is the gravity vector, $\boldsymbol{\tau}$ is the tensor of the viscous stresses,

$$\boldsymbol{\tau} = \mu \left(\nabla \mathbf{u} + \nabla \mathbf{u}^T \right) - \frac{2}{3} \mu (\nabla \cdot \mathbf{u}) \mathbf{I}, \tag{4}$$

and $\mathbf{q}$ denotes the heat flux,

$$\mathbf{q} = -\lambda \nabla \theta. \tag{5}$$

Here, θ is the temperature and λ denotes the thermal conductivity. In this paper we use the simple ideal gas equation of state (EOS) to close the system:

$$p = \rho R \theta, \tag{6}$$

where $R = c_p - c_v$ is the specific gas constant, with c_p being the heat capacity at constant pressure, while c_v denotes the heat capacity at constant volume. Accounting for (6), the relation between the total energy, the kinetic energy k and the specific internal energy e reads

$$\rho E = \rho e + \rho k = \frac{1}{\gamma - 1} p + \frac{1}{2} \rho \left| \mathbf{u} \right|^2 \tag{7}$$

with $\gamma = \frac{c_p}{c_v}$ being the ratio of specific heats. Introducing the enthalpy,

$$h = e + \frac{p}{\rho} = \frac{\gamma}{\gamma - 1} \frac{p}{\rho} \tag{8}$$

we get

$$\frac{\partial \rho E}{\partial t} + \nabla \cdot (\rho k \mathbf{u}) + \nabla \cdot (\rho h \mathbf{u}) - \nabla \cdot (\boldsymbol{\tau} \mathbf{u}) + \nabla \cdot \mathbf{q} = \rho \mathbf{g} \cdot \mathbf{u}. \tag{9}$$

The former system, (1)-(3), can be rewritten in terms of the conservative variables, $\mathbf{w} = (w_\rho, \mathbf{w_u}, w_E)^T = (\rho, \rho \mathbf{u}, \rho E)^T$ as

$$\frac{\partial w_\rho}{\partial t} + \nabla \cdot (\mathbf{w_u}) = 0, \tag{10}$$

$$\frac{\partial \mathbf{w_u}}{\partial t} + \nabla \cdot \left(\frac{1}{\rho} \mathbf{w_u} \otimes \mathbf{w_u} \right) + \nabla p - \nabla \cdot \boldsymbol{\tau} = \rho \mathbf{g}, \tag{11}$$

$$\frac{\partial w_E}{\partial t} + \nabla \cdot \left[\frac{1}{\rho} \mathbf{w_u} (w_E + p) \right] - \nabla \cdot \left(\frac{1}{\rho} \boldsymbol{\tau} \mathbf{w_u} \right) + \nabla \cdot \mathbf{q} = \mathbf{g} \cdot \mathbf{w_u}. \tag{12}$$

3. Numerical method

Discretization of system (10)-(12) is performed extending the hybrid finite volume / finite element method proposed in [81, 85, 1, 86]. We start by considering a semi-discrete scheme where only time discretization is applied leading to

$$\frac{1}{\Delta t} \left(W_\rho^{n+1} - W_\rho^n \right) + \nabla \cdot (\mathbf{W}_\mathbf{u}^n) = 0, \tag{13}$$

$$\frac{1}{\Delta t} \left(\mathbf{W}_\mathbf{u}^{n+1} - \mathbf{W}_\mathbf{u}^n \right) + \nabla \cdot \left(\frac{1}{\rho^n} \mathbf{W}_\mathbf{u}^n \otimes \mathbf{W}_\mathbf{u}^n \right) + \nabla P^{n+1} - \nabla \cdot \mathbf{T}^n = \rho^n \mathbf{g}, \tag{14}$$

$$\frac{1}{\Delta t} \left(W_E^{n+1} - W_E^n \right) + \nabla \cdot (K^n \mathbf{W}_\mathbf{u}^n) + \nabla \cdot \left(H^{n+1} \mathbf{W}_\mathbf{u}^{n+1} \right) - \nabla \cdot \left(\frac{1}{\rho^n} \mathbf{T}^n \mathbf{W}_\mathbf{u}^n \right) + \nabla \cdot \mathbf{Q}^n = \mathbf{g} \cdot \mathbf{W}_\mathbf{u}^n, \tag{15}$$

with $\mathbf{W}^n$, P^n approximations of the solution, $\mathbf{w}(\mathbf{x}, t^n)$, $p(\mathbf{x}, t^n)$, at time $t^n \in \mathbb{R}^+$ and $\mathbf{x} \in \mathbb{R}^d$ the spatial coordinate. We now introduce the following notation for an intermediate approximation of the linear momentum

$$\widetilde{\mathbf{W}}_\mathbf{u} = \mathbf{W}_\mathbf{u}^n - \Delta t \left(\nabla \cdot \left(\frac{1}{\rho^n} \mathbf{W}_\mathbf{u}^n \otimes \mathbf{W}_\mathbf{u}^n \right) - \nabla \cdot \mathbf{T}^n - \rho^n \mathbf{g} \right) \tag{16}$$

and define

$$\widetilde{\widetilde{\mathbf{W}}}_\mathbf{u} := \widetilde{\mathbf{W}}_\mathbf{u} - \Delta t \nabla P^n, \qquad \delta P^{n+1} := P^{n+1} - P^n \tag{17}$$

so

$$\widetilde{\mathbf{W}}_\mathbf{u} = \widetilde{\widetilde{\mathbf{W}}}_\mathbf{u} + \Delta t \nabla P^n, \tag{18}$$

$$\mathbf{W}_{\mathbf{u}}^{n+1} = \widetilde{\mathbf{W}}_{\mathbf{u}} - \Delta t \nabla P^{n+1} = \widetilde{\widetilde{\mathbf{W}}}_{\mathbf{u}} - \Delta t \nabla \delta P^{n+1}. \tag{19}$$

In such a way, we have derived a pressure-correction formulation in which the computation of the pressure and the linear momentum are "decoupled". Similarly, we can define an intermediate auxiliary variable for the computation of the total energy,

$$\widetilde{W}_E = W_E^n - \Delta t \left(\nabla\cdot \left(K^n \mathbf{W}_{\mathbf{u}}^n\right) - \nabla\cdot \left(\frac{1}{\rho^n} \mathbf{T}^n \mathbf{W}_{\mathbf{u}}^n \right) + \nabla\cdot \mathbf{Q}^n - \mathbf{g}\cdot \mathbf{W}_{\mathbf{u}}^n \right). \tag{20}$$

Later, W_E^{n+1} would be recovered from

$$W_E^{n+1} = \widetilde{W}_E - \Delta t \nabla\cdot \left(H^{n+1} \mathbf{W}_{\mathbf{u}}^{n+1} \right). \tag{21}$$

On the other hand, equation (15) can be rewritten in terms of the pressure and the kinetic energy by using relation (7) and the ideal gas equation of state as follows:

$$\frac{P^{n+1}}{\gamma-1} + (\rho K)^{n+1} = \frac{P^n}{\gamma-1} - \frac{P^n}{\gamma-1} + \widetilde{W}_E - \Delta t \nabla\cdot \left(H^{n+1} \mathbf{W}_{\mathbf{u}}^{n+1} \right) \tag{22}$$

Substitution of (19) yields

$$\frac{P^{n+1}}{\gamma-1} - \frac{P^n}{\gamma-1} = -(\rho K)^{n+1} + \widetilde{W}_E - \frac{P^n}{\gamma-1} - \Delta t \nabla\cdot \left(H^{n+1} \widetilde{\widetilde{\mathbf{W}}}_{\mathbf{u}} \right) + \Delta t^2 \nabla\cdot \left(H^{n+1} \nabla \delta P^{n+1} \right). \tag{23}$$

Hence,

$$\frac{1}{\gamma-1} \delta P^{n+1} - \Delta t^2 \nabla\cdot \left(H^{n+1} \nabla \delta P^{n+1} \right) = \widetilde{W}_E - \frac{P^n}{\gamma-1} - (\rho K)^{n+1} - \Delta t \nabla\cdot \left(H^{n+1} \widetilde{\widetilde{\mathbf{W}}}_{\mathbf{u}} \right). \tag{24}$$

A Picard procedure is applied to deal with the crossed t^{n+1} terms, i.e., P^{n+1} in equation (19), $(\rho K)^{n+1} = \frac{1}{2\rho^{n+1}} \left| \mathbf{W}_{\mathbf{u}}^{n+1} \right|^2$ and H^{n+1} in (24), and $\mathbf{W}_{\mathbf{u}}^{n+1}$ in (21), since we do not want to solve a highly nonlinear system. The final system of equations to be discretized in space reads

$$W_\rho^{n+1} = W_\rho^n - \Delta t \nabla\cdot \left(\mathbf{W}_{\mathbf{u}}^n \right), \tag{25}$$

$$\widetilde{\widetilde{\mathbf{W}}}_{\mathbf{u}} = \mathbf{W}_{\mathbf{u}}^n - \Delta t \left(\nabla\cdot \left(\frac{1}{\rho^n} \mathbf{W}_{\mathbf{u}}^n \otimes \mathbf{W}_{\mathbf{u}}^n \right) + \nabla P^n - \nabla\cdot \mathbf{T}^n - \rho^n \mathbf{g} \right), \tag{26}$$

$$\widetilde{W}_E = W_E^n - \Delta t \left(\nabla\cdot \left(K^n \mathbf{W}_{\mathbf{u}}^n\right) - \nabla\cdot \left(\frac{1}{\rho^n} \mathbf{T}^n \mathbf{W}_{\mathbf{u}}^n \right) + \nabla\cdot \mathbf{Q}^n - \mathbf{g}\cdot \mathbf{W}_{\mathbf{u}}^n \right), \tag{27}$$

$$\frac{1}{\gamma-1} \delta P^{n+1,k+1} - \Delta t^2 \nabla\cdot \left(H^{n+1,k} \nabla \delta P^{n+1,k+1} \right) = \widetilde{W}_E - \frac{P^n}{\gamma-1} - (\rho K)^{n+1,k} - \Delta t \nabla\cdot \left(H^{n+1,k} \widetilde{\widetilde{\mathbf{W}}}_{\mathbf{u}} \right), \tag{28}$$

$$\mathbf{W}_{\mathbf{u}}^{n+1,k+1} = \widetilde{\widetilde{\mathbf{W}}}_{\mathbf{u}} - \Delta t \nabla \delta P^{n+1,k+1}, \tag{29}$$

$$P^{n+1,k+1} = P^n + \delta P^{n+1,k+1}, \tag{30}$$

$$W_E^{n+1} = \widetilde{W}_E - \Delta t \nabla\cdot \left(H^{n+1,k+1} \mathbf{W}_{\mathbf{u}}^{n+1,k+1} \right), \tag{31}$$

with k the Picard iteration index, $k = 1, \ldots, N_{\text{Pic}}$.

Let us remark that the method is by construction asymptotic preserving in the low Mach number limit. In the limit $M \to 0$, we have $c^2 \to \infty$ with $c^2 = \frac{H}{\gamma-1}$. According to [2, 3], the pressure, and for constant density also the enthalpy, tend to a constant. In this limit, we can now divide equation (28) by the enthalpy and neglecting terms of the order $1/c^2$ we obtain the following equation

$$\nabla^2 \delta P^{n+1} = \frac{1}{\Delta t} \nabla\cdot \left(\widetilde{\widetilde{\mathbf{W}}}_{\mathbf{u}} \right), \tag{32}$$

which, together with the momentum equation (26), corresponds to the pressure correction system obtained for the incompressible Navier-Stokes equations in [1].

For general equations of state, relation (24) needs to be replaced by

$$W_E(P^{n+1}, W_\rho^{n+1}) - \Delta t^2 \nabla\cdot\left(H^{n+1}\nabla P^{n+1}\right) = \widetilde{W}_E - (\rho K)^{n+1} - \Delta t \nabla\cdot\left(H^{n+1}\widetilde{\widetilde{\mathbf{W}}}_{\mathbf{u}}\right), \tag{33}$$

where the density at the new time t^{n+1} is readily available from eqn. (25), and thus the only unknown remains the scalar pressure field P^{n+1} at the new time, see also [39]. When appropriate mass-lumping is used within a finite-element discretization of (33), the resulting mildly nonlinear pressure system can be solved very efficiently at the aid of the (nested) Newton-type methods of Brugnano and Casulli [87, 88, 89] and Casulli and Zanolli [90, 91], and for which convergence has been rigorously proven. For finite elements without mass lumping, i.e., for non-diagonal mass matrices, the theorems which are the basis of the convergence proofs in the aforementioned works of Casulli *et al.* do *not* directly apply and still need to be generalized to more general non-diagonal but symmetric positive definite mass matrices. In the rest of this paper, we therefore assume that the simple ideal gas equation of state holds.

Spatial discretization is done by choosing a numerical method adapted to the nature of each equation: finite volumes are applied to approximate the transport-diffusion equations, whereas the Poisson problem is solved using continuous finite elements. The use of staggered grids avoids the checker-board phenomena, which are typical for many numerical methods on collocated grids. The use of unstructured meshes increases the applicability of the methodology with respect to Cartesian grids since the meshing of complex domains becomes straightforward. The overall algorithm can be divided into four main stages:

- Transport-diffusion stage. The equations (25), (26), and (27) are solved using explicit finite volumes in the dual mesh. To attain second order in space and time, a local ADER method combined with an ENO reconstruction is considered. Within this stage we get the new density, ρ^{n+1}, and the intermediate approximations of the momentum, $\widetilde{\widetilde{\mathbf{W}}}_{\mathbf{u}}$, as well as the total energy density, $\widetilde{W}_E$ at each cell of the dual mesh.

- Pre-projection stage. The intermediate states for the total energy density and for the linear momentum are transferred from the dual to the primal grid. Next, the auxiliary variables that will be needed within the next stage, as the enthalpy, $H^{n+1,k}$, and the kinetic energy density, $(\rho K)^{n+1,k}$, are also computed. Let us note that the intermediate variables are calculated only once per time step, meanwhile the auxiliary variables are updated at each Picard iteration.

- Projection stage. A $\mathbb{P}^1$ finite element scheme is employed in order to solve the pressure equation (28) implicitly. The resulting $\delta P^{n+1,k+1}$ is computed on the vertexes of the primal simplex mesh.

- Post-projection stage. The pressure correction at the new time t^{n+1} is substituted in (29) and (30) to update the linear momentum $\mathbf{W}_{\mathbf{u}}^{n+1,k+1}$ and the pressure $P^{n+1,k+1}$. Once the Picard iterations have finished, the total energy, W_E^{n+1}, is recovered following (31).

In what follows, we will further detail each stage of the algorithm.

3.1. Staggered unstructured mesh

In this paper we make use of two overlapping unstructured staggered meshes to discretize the domain Ω. For the sake of simplicity, we focus here on the 2D case introducing the main notation needed. Further details on the construction of three-dimensional face-type staggered meshes can be found in [81, 65, 1, 69, 86].

Let us consider a triangular primal mesh $\{T_k,\, k = 1, \ldots, nel\}$ with vertex $\{V_j,\, j = 1, \ldots, nver\}$ (Figure 1 left). We now define the two triangles with basis one interior edge of a primal element and opposite vertex the barycenters, B, B', of the two primal elements sharing this face. The dual element, C_i, is then built by merging these two triangles (Figure 1 center). Similarly, a dual boundary element is a triangle which has as basis a primal boundary edge and as opposite vertex the barycenter of the primal element. Let us note that on the dual mesh the nodes $\{N_i,\, i = 1, \ldots, nnod\}$ are associated with the edges/faces of the simplex elements on the primal mesh. The remaining notation related to the mesh is as follows:

- $\mathcal{K}_i$ is the set of neighbouring nodes of a node N_i consisting of the barycenters of the dual cells sharing a face with C_i.
- Γ_i is the boundary of a cell C_i and $\widetilde{\boldsymbol{\eta}}_i$ its outward unit normal.
- Γ_{ij} is the edge between cells C_i and C_j. N_{ij} is the barycenter of Γ_{ij} (Figure 1 right). Note that $\Gamma_i = \bigcup_{N_j \in \mathcal{K}_i} \Gamma_{ij}$.
- $|C_i|$ is the area of C_i.
- $\widetilde{\boldsymbol{\eta}}_{ij}$ is the outward unit normal vector to Γ_{ij}. We define $\boldsymbol{\eta_{ij}} := \widetilde{\boldsymbol{\eta}}_{\boldsymbol{ij}} ||\boldsymbol{\eta_{ij}}||$, where, $||\boldsymbol{\eta_{ij}}||$ represents the length of Γ_{ij}.

Sketches of the 2D and 3D staggered meshes are depicted in Figures 1 and 2, respectively.

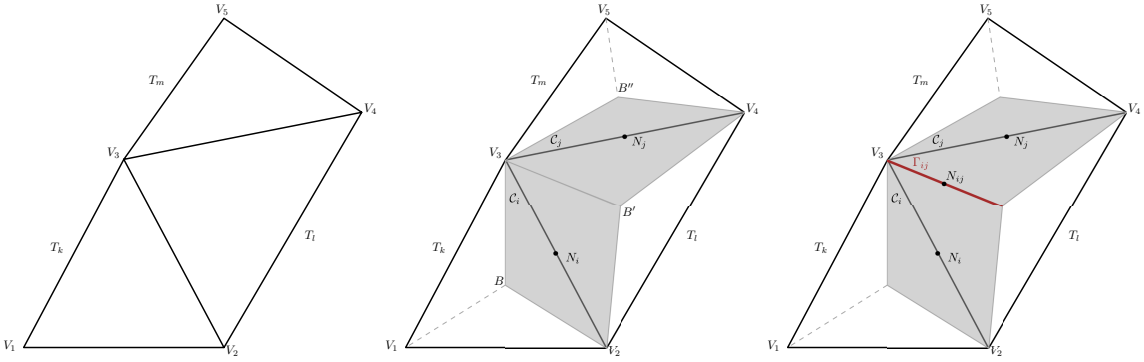

Figure 1: Construction of face-type dual elements from a 2D primal mesh. Left: primal mesh made of elements T_k, T_l, T_m and vertex V_n, $n = 1, \ldots, 5$. Center: dual interior cells C_i, C_j (shadowed in grey), white triangles correspond to boundary cells. Right: boundary face, Γ_{ij}, between the dual elements C_i, C_j.

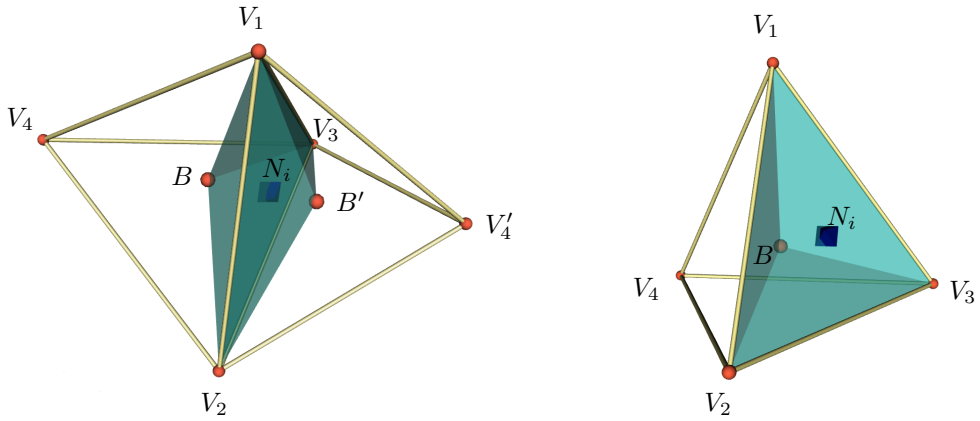

Figure 2: Example of an interior finite volume (left) and of a boundary finite volume (right) which constitute the staggered dual mesh in three space dimensions.

3.2. Transport-diffusion stage

To solve the transport dominated equations, we use a finite volume method on the dual grid. As result, we will obtain the value of the averaged new density, $W_\rho^{n+1} = \rho^{n+1}$, on each dual cell, as well as

intermediate approximations for the cell averaged linear momentum, $\widetilde{\widetilde{\mathbf{W}}}_{\mathbf{u}}$, and total energy density, $\widetilde{W}_E$. We start integrating equations (25)-(27) on each dual cell C_i and applying Gauss theorem which yields

$$\rho_i^{n+1} = \rho_i^n - \frac{\Delta t}{|C_i|}\int_{\Gamma_i} \mathcal{F}^{W_\rho}\left(\mathbf{W}^n\right)\widetilde{\boldsymbol{\eta}}_i\, dS, \tag{34}$$

$$\widetilde{\widetilde{\mathbf{W}}}_{\mathbf{u},\,i} = \mathbf{W}^n_{\mathbf{u},\,i} - \frac{\Delta t}{|C_i|}\left(\int_{\Gamma_i} \mathcal{F}^{\mathbf{W}_\mathbf{u}}\left(\mathbf{W}^n\right)\widetilde{\boldsymbol{\eta}}_i\, dS + \int_{C_i} \nabla P^n dV - \int_{\Gamma_i} \mathbf{T}^n\,\widetilde{\boldsymbol{\eta}}_i\, dS - \int_{C_i} \rho^n \mathbf{g} dV\right), \tag{35}$$

$$\widetilde{W}_{E,i} = W^n_{E,i} - \frac{\Delta t}{|C_i|}\left(\int_{\Gamma_i} \mathcal{F}^{W_E}\left(\mathbf{W}^n\right)\cdot\widetilde{\boldsymbol{\eta}}_i\, dS - \int_{\Gamma_i}\left(\frac{1}{\rho^n}\mathbf{T}^n\mathbf{W}^n_{\mathbf{u}}\right)\cdot\widetilde{\boldsymbol{\eta}}_i\, dS + \int_{\Gamma_i}\mathbf{Q}^n\cdot\widetilde{\boldsymbol{\eta}}_i\, dS - \int_{C_i}\mathbf{g}\cdot\mathbf{W}^n_{\mathbf{u}} dV\right). \tag{36}$$

where

$$\mathcal{F}^{W_\rho}(\mathbf{W}^n) := \mathbf{W}^n_{\mathbf{u}}, \qquad \mathcal{F}^{\mathbf{W}_\mathbf{u}}(\mathbf{W}^n) := \frac{1}{\rho^n}\mathbf{W}^n_{\mathbf{u}}\otimes\mathbf{W}^n_{\mathbf{u}}, \qquad \mathcal{F}^{W_E}(\mathbf{W}^n) := K^n\mathbf{W}^n_{\mathbf{u}} \tag{37}$$

are the convective fluxes of mass, momentum, and total energy, respectively.

3.2.1. Convective numerical fluxes

The global normal flux through the boundary of a dual cell is denoted by

$$\mathcal{Z}(\mathbf{W}^n, \tilde{\boldsymbol{\eta}}_i) := \mathcal{F}(\mathbf{W}^n)\tilde{\boldsymbol{\eta}}_i, \quad \text{with} \quad \mathcal{F}(\mathbf{W}^n) = \left(\mathcal{F}^{W_\rho}(\mathbf{W}^n), \mathcal{F}^{\mathbf{W}_\mathbf{u}}(\mathbf{W}^n), \mathcal{F}^{W_E}(\mathbf{W}^n)\right)^T. \tag{38}$$

Let us recall that the flux contribution in the energy equation accounts only for the kinetic energy density contribution, ρk, instead of the total energy density, ρE. Within the flux computation the value of K^n is recovered from the linear momentum and density fields, $K^n = \frac{1}{2\rho^n}\left|\mathbf{W}^n_{\mathbf{u}}\right|^2$. The integral of the flux term on Γ_i can be split into the sum of the integral on the cell faces, Γ_{ij},

$$\int_{\Gamma_i}\mathcal{F}(\mathbf{W}^n)\widetilde{\boldsymbol{\eta}}_i\,\mathrm{dS} = \sum_{N_j\in\mathcal{K}_i}\int_{\Gamma_{ij}}\mathcal{Z}(\mathbf{W}^n, \tilde{\boldsymbol{\eta}}_{ij})\,\mathrm{dS}, \tag{39}$$

and approximated using an upwind scheme to get a stable discretization. In particular, we consider a modified Rusanov flux function, [92, 86],

$$\begin{aligned}\boldsymbol{\phi}\left(\mathbf{W}^n_i, \mathbf{W}^n_j, \boldsymbol{\eta}_{ij}\right) &= \left(\phi_\rho\left(\mathbf{W}^n_i, \mathbf{W}^n_j, \boldsymbol{\eta}_{ij}\right), \boldsymbol{\phi}_{\mathbf{u}}\left(\mathbf{W}^n_i, \mathbf{W}^n_j, \boldsymbol{\eta}_{ij}\right), \phi_E\left(\mathbf{W}^n_i, \mathbf{W}^n_j, \boldsymbol{\eta}_{ij}\right)\right)^T \\ &= \frac{1}{2}(\mathcal{Z}(\mathbf{W}^n_i, \boldsymbol{\eta}_{ij}) + \mathcal{Z}(\mathbf{W}^n_j, \boldsymbol{\eta}_{ij})) - \frac{1}{2}\alpha^n_{RS,\,ij}\left(\boldsymbol{\mathcal{W}}^n_j - \boldsymbol{\mathcal{W}}^n_i\right)\end{aligned} \tag{40}$$

with

$$\boldsymbol{\mathcal{W}} := (W_\rho, \mathbf{W}_\mathbf{u}, \rho K)^T \tag{41}$$

the modified conservative variables vector,

$$\alpha^n_{RS,\,ij} = \alpha_{RS}(\mathbf{W}^n_i, \mathbf{W}^n_j, \boldsymbol{\eta}_{ij}) := \max\left\{\left|\mathbf{U}^n_i\cdot\boldsymbol{\eta}_{ij}\right|, \left|\mathbf{U}^n_j\cdot\boldsymbol{\eta}_{ij}\right|\right\} + c_\alpha\left\|\boldsymbol{\eta}_{ij}\right\| \tag{42}$$

the maximum signal speed on the edge and $c_\alpha \in \mathbb{R}^+_0$ an artificial viscosity coefficient that may be activated on particular tests to increase the stability properties of the final scheme when large variations of the density and energy fields are encountered in the presence of small velocities. Substitution in (34)-(36) gives

$$\rho_i^{n+1} = \rho_i^n - \frac{\Delta t}{|C_i|}\sum_{N_j\in\mathcal{K}_i}\phi_\rho\left(\mathbf{W}^n_i, \mathbf{W}^n_j, \boldsymbol{\eta}_{ij}\right), \tag{43}$$

$$\widetilde{\widetilde{\mathbf{W}}}_{\mathbf{u},\,i} = \mathbf{W}^n_{\mathbf{u},\,i} - \frac{\Delta t}{|C_i|}\left(\sum_{N_j\in\mathcal{K}_i}\boldsymbol{\phi}_{\mathbf{u}}\left(\mathbf{W}^n_i,\mathbf{W}^n_j,\boldsymbol{\eta}_{ij}\right) + \int_{C_i}\nabla P^n dV - \int_{\Gamma_i}\mathbf{T}^n\,\widetilde{\boldsymbol{\eta}}_i\,dS - \int_{C_i}\rho^n\mathbf{g}dV\right), \tag{44}$$

$$\widetilde{W}_{E,i} = W^n_{E,i} - \frac{\Delta t}{|C_i|}\left(\sum_{N_j\in\mathcal{K}_i}\phi_E\left(\mathbf{W}^n_i,\mathbf{W}^n_j,\boldsymbol{\eta}_{ij}\right) - \int_{\Gamma_i}\left(\frac{1}{\rho^n}\mathbf{T}^n\mathbf{W}^n_{\mathbf{u}}\right)\cdot\widetilde{\boldsymbol{\eta}}_i\,dS + \int_{\Gamma_i}\mathbf{Q}^n\cdot\widetilde{\boldsymbol{\eta}}_i\,dS - \int_{C_i}\mathbf{g}\cdot\mathbf{W}^n_{\mathbf{u}}dV\right). \tag{45}$$

The scheme proposed above would result in a first order scheme in space and time. To increase the order of accuracy attaining second order in space and time, a local ADER methodology (LADER) is employed, see [1, 93, 86]. The reader is referred to [94, 29, 95, 84] for further details on the original ADER methodology and to [96, 97, 72] for an alternative variant of ADER schemes that allow to avoid the cumbersome Cauchy-Kovalevskaya procedure thanks to the use of a general space-time finite element predictor. In what follows, we briefly recall the main steps to be performed in the LADER algorithm:

Step 1. Piecewise polynomial reconstruction in the neighbourhood of each boundary edge of the cell. Considering an scalar conservative variable, W, and one of the cell boundaries, Γ_{ij}, the related reconstruction polynomials read

$$P^i_{ij}(N) = W_i + (N - N_i)\,(\nabla\,W)^i_{ij}\,, \quad P^j_{ij}(N) = W_j + (N - N_j)\,(\nabla\,W)^j_{ij}\,. \tag{46}$$

To circumvent Godunov's theorem and to develop a second order scheme avoiding spurious oscillations, we introduce a non linearity via the use of a nonlinear Essentially Non-Oscillatory (ENO) reconstruction. Accordingly, the gradients are computed as

$$(\nabla\,W)^i_{ij} = \begin{cases} (\nabla\,W)_{T_{ijL}}\,, & \text{if } \left|(\nabla\,W)_{T_{ijL}}\cdot(N_{ij}-N_i)\right| \le \left|(\nabla\,W)_{T_{ij}}\cdot(N_{ij}-N_i)\right|, \\ (\nabla\,W)_{T_{ij}}\,, & \text{otherwise;} \end{cases}$$

$$(\nabla\,W)^j_{ij} = \begin{cases} (\nabla\,W)_{T_{ijR}}\,, & \text{if } \left|(\nabla\,W)_{T_{ijR}}\cdot(N_{ij}-N_j)\right| \le \left|(\nabla\,W)_{T_{ij}}\cdot(N_{ij}-N_j)\right|, \\ (\nabla\,W)_{T_{ij}}\,, & \text{otherwise,} \end{cases}$$

with T_{ij}, T_{ijL} and T_{ijR} the centered and upwind primal elements to the face Γ_{ij} where the gradients are computed using a Galerkin approach (Crouzeix-Raviart finite elements). An alternative to the ENO-based reconstruction is the use of classical slope limiters like the Barth and Jespersen limiter [98], or the minmod limiter of Roe [99, 29]. Also, *a posteriori* limiting strategies like the MOOD approach, [100], could be used and will be part of future research.

Step 2. Calculation of the necessary boundary–extrapolated data in $\mathbf{x}_{N_{ij}}$ of each edge/face of the FV mesh,

$$W_{i\,N_{ij}} = p^i_{ij}(N_{ij}) = W_i + (N_{ij} - N_i)\,(\nabla\,W)^i_{ij}\,, \tag{47}$$

$$W_{j\,N_{ij}} = p^j_{ij}(N_{ij}) = W_j + (N_{ij} - N_j)\,(\nabla\,W)^j_{ij}\,. \tag{48}$$

Step 3. Use of the mid-point rule to get a second order of accuracy approximation in time. A temporal Taylor series expansion in combination with the Cauchy-Kovalevskaya procedure, based on the mass, momentum, and energy equations (10), (11), (28), are employed in order to approximate the conservative variables at the time $t^n + \frac{\Delta t}{2}$:

$$\overline{\mathbf{W}}_{i\,N_{ij}} = \rho_{i\,N_{ij}} + \mathbf{W}^*_{N_{ij}}, \qquad \overline{\mathbf{W}}_{j\,N_{ij}} = \rho_{j\,N_{ij}} + \mathbf{W}^*_{N_{ij}} \tag{49}$$

where

$$\mathbf{W}^*_{\rho\,N_{ij}} \;:=\; -\frac{\Delta t}{2\mathcal{L}_{ij}}\left[\mathcal{Z}^\rho(\mathbf{W}_{i\,N_{ij}},\boldsymbol{\eta}_{ij}) + \mathcal{Z}^\rho(\mathbf{W}_{j\,N_{ij}},\boldsymbol{\eta}_{ij})\right], \tag{50}$$

$$\begin{aligned}\mathbf{W}^{*}_{\mathbf{u}\,N_{ij}} &:= -\frac{\Delta t}{2\mathcal{L}_{ij}}\left[\mathcal{Z}^{\mathbf{u}}(\mathbf{W}_{i\,N_{ij}},\boldsymbol{\eta}_{ij})+\mathcal{Z}^{\mathbf{u}}(\mathbf{W}_{j\,N_{ij}},\boldsymbol{\eta}_{ij})\right]+\frac{\Delta t}{2\mathcal{L}_{ij}}\mathbf{T}^{*}\boldsymbol{\eta}_{ij}\\ &\quad -\frac{\Delta t}{2}\left(\nabla\, P\right)_{T_{ij}}+\frac{\Delta t}{4}\left(\rho_{i\,N_{ij}}+\rho_{j\,N_{ij}}\right)\mathbf{g}, \qquad (51)\\ W^{*}_{E\,N_{ij}} &:= -\frac{\Delta t}{2\mathcal{L}_{ij}}\left[\mathcal{Z}^{E}(\mathbf{W}_{i\,N_{ij}},\boldsymbol{\eta}_{ij})+\mathcal{Z}^{E}(\mathbf{W}_{j\,N_{ij}},\boldsymbol{\eta}_{ij})\right]+\frac{\Delta t}{2\mathcal{L}_{ij}}\left(\mathbf{TU}\right)^{*}\cdot\boldsymbol{\eta}_{ij}\\ &\quad +\frac{\Delta t}{4}\mathbf{g}\cdot\left(\mathbf{W}_{\mathbf{u}\,i\,N_{ij}}+\mathbf{W}_{\mathbf{u},j\,N_{ij}}\right), \qquad (52)\end{aligned}$$

with

$$\mathbf{T}^{*}=\mu\left[\left(\nabla\,\mathbf{W}_{\mathbf{u}}+\nabla\,\mathbf{W}_{\mathbf{u}}^{T}\right)_{i\,N_{ij}}+\left(\nabla\,\mathbf{W}_{\mathbf{u}}+\nabla\,\mathbf{W}_{\mathbf{u}}^{T}\right)_{j\,N_{ij}}-\frac{2}{3}\left(\nabla\cdot\mathbf{W}_{\mathbf{u},\,i\,N_{ij}}\mathbf{I}+\nabla\cdot\mathbf{W}_{\mathbf{u},\,j\,N_{ij}}\mathbf{I}\right)\right], \qquad (53)$$

$$\begin{aligned}\left(\mathbf{TU}\right)^{*}=\mu\Bigg[&\left(\nabla\,\mathbf{W}_{\mathbf{u}}+\nabla\,\mathbf{W}_{\mathbf{u}}^{T}\right)_{i\,N_{ij}}\mathbf{U}_{i\,N_{ij}}+\left(\nabla\,\mathbf{W}_{\mathbf{u}}+\nabla\,\mathbf{W}_{\mathbf{u}}^{T}\right)_{j\,N_{ij}}\mathbf{U}_{j\,N_{ij}}\\ &-\frac{2}{3}\left(\nabla\cdot\mathbf{W}_{\mathbf{u},\,i\,N_{ij}}\mathbf{U}_{i\,N_{ij}}+\nabla\cdot\mathbf{W}_{\mathbf{u},\,j\,N_{ij}}\mathbf{U}_{j\,N_{ij}}\right)\Bigg]. \qquad (54)\end{aligned}$$

Step 4. Calculation of the numerical flux for the convective terms using (40),

$$\boldsymbol{\phi}\left(\overline{\mathbf{W}}^{n}_{i\,N_{ij}},\overline{\mathbf{W}}^{n}_{j\,N_{ij}},\boldsymbol{\eta}_{ij}\right)=\frac{1}{2}\left[\mathcal{Z}(\overline{\mathbf{W}}^{n}_{i\,N_{ij}},\boldsymbol{\eta}_{ij})+\mathcal{Z}(\overline{\mathbf{W}}^{n}_{j\,N_{ij}},\boldsymbol{\eta}_{ij})\right]-\frac{1}{2}\overline{\alpha}^{n}_{RS,\,ij}\left(\overline{\boldsymbol{\mathcal{W}}}^{n}_{j\,N_{ij}}-\overline{\boldsymbol{\mathcal{W}}}^{n}_{i\,N_{ij}}\right). \qquad (55)$$

3.2.2. Viscous term

Gauss' theorem allows to rewrite the volume integrals of the viscous stress tensor and of the heat flux into surface integrals over the boundary, Γ_i, which can further be rewritten as a sum of integrals over the individual cell faces, Γ_{ij}. This leads to

$$\int_{C_i}\nabla\cdot\mathbf{T}^{n}dV=\sum_{N_j\in\mathcal{K}_i}\int_{\Gamma_{ij}}\mathbf{T}^{n}\widetilde{\boldsymbol{\eta}}_{ij}\,\mathrm{dS}=\sum_{N_j\in\mathcal{K}_i}\int_{\Gamma_{ij}}\mu\left[\nabla\,\mathbf{U}^{n}+\left(\nabla\,\mathbf{U}^{n}\right)^{T}-\frac{2}{3}\nabla\cdot\mathbf{U}^{n}I\right]\widetilde{\boldsymbol{\eta}}_{ij}\,\mathrm{dS}, \qquad (56)$$

$$\int_{C_i}\nabla\cdot\left(\frac{1}{\rho^{n}}\mathbf{T}^{n}\mathbf{W}^{n}_{\mathbf{u}}\right)dV=\sum_{N_j\in\mathcal{K}_i}\int_{\Gamma_{ij}}\frac{1}{\rho^{n}}\mathbf{T}^{n}\mathbf{W}^{n}_{\mathbf{u}}\cdot\widetilde{\boldsymbol{\eta}}_{ij}\,\mathrm{dS}=\sum_{N_j\in\mathcal{K}_i}\int_{\Gamma_{ij}}\mu\left[\left(\nabla\,\mathbf{U}^{n}+\left(\nabla\,\mathbf{U}^{n}\right)^{T}-\frac{2}{3}\nabla\cdot\mathbf{U}^{n}I\right)\mathbf{U}^{n}\right]\cdot\widetilde{\boldsymbol{\eta}}_{ij}\,\mathrm{dS}, \qquad (57)$$

where the gradients are computed on the primal element containing the face, T_{ij}, following the Galerkin approach already introduced in Section 3.2.1 within the LADER reconstruction. The corresponding numerical diffusion functions read

$$\varphi_{\mathbf{u}}\left(\mathbf{U}^{n}_{i},\mathbf{U}^{n}_{j},\boldsymbol{\eta}_{ij}\right)\approx\int_{\Gamma_{ij}}\mu\left[\nabla\,\mathbf{U}^{n}+\left(\nabla\,\mathbf{U}^{n}\right)^{T}-\frac{2}{3}\nabla\cdot\mathbf{U}^{n}\right]\widetilde{\boldsymbol{\eta}}_{ij}\mathrm{dS}, \qquad (58)$$

$$\varphi_{E}\left(\mathbf{U}^{n}_{i},\mathbf{U}^{n}_{j},\boldsymbol{\eta}_{ij}\right)\approx\int_{\Gamma_{ij}}\mu\left[\left(\nabla\,\mathbf{U}^{n}+\left(\nabla\,\mathbf{U}^{n}\right)^{T}-\frac{2}{3}\nabla\cdot\mathbf{U}^{n}I\right)\mathbf{U}^{n}\right]\cdot\widetilde{\boldsymbol{\eta}}_{ij}\mathrm{dS}. \qquad (59)$$

Similar to what has been done for the advection term, a Taylor series expansion combined with the Cauchy-Kovalevskaya procedure could be applied to get a second order accurate approximation of the viscous terms in space and time. The main difference with respect to the flux terms computation is that we now can neglect the presence of the flux term on the reconstruction of the linear momentum field. As it has been shown in [1] for the scalar advection-diffusion-reaction equation, the specific way of computing the gradients makes the mixed contribution of advection and diffusion terms be completely included in the time evolution of the flux to the half time level. We should notice that the evolution of viscous terms may lead to a more restrictive CFL stability condition, so the time step would be smaller than when applying LADER only to convective terms, see [84]. Once the evolution to the half time level of the linear momentum, $\overline{\overline{\mathbf{W}}}^{n}_{\mathbf{u},\,i}$, is computed, it is divided by the reconstructed density to approximate the evolved velocity, $\overline{\overline{\mathbf{U}}}^{n}_{i}=\left(\overline{\rho}^{n}_{i}\right)^{-1}\overline{\overline{\mathbf{W}}}^{n}_{\mathbf{u},\,i}$, to be inserted in (58)-(59).

3.2.3. Pressure term

To account for the pressure contribution at the previous time step, we transform the integral of its gradient on the dual cell into the sum of the normal projection on each face

$$\int_{C_i} \nabla P^n dV = \sum_{N_j \in \mathcal{K}_i} P^n_{ij} \boldsymbol{\eta_{ij}}. \tag{60}$$

The value of the pressure at each dual face, P^n_{ij}, is obtained as the average of the pressure at its vertexes. Regarding the vertex corresponding to the barycenter of the primal element, the pressure is approximated again as the averaged value on the nodes of the primal element. To get second order in space and time, the pressure in (60) is replaced by its half in time reconstructed value. The LADER methodology is applied like for the viscous term computation to get also the value of $\overline{\overline{\mathbf{W}}}^n_{E,\,i}$ from which the evolved pressure $\overline{\overline{P}}^n_{ij}$ can be recovered using relation (7).

3.2.4. Gravity term

The gravity source terms in (26)-(27) are integrated on each spatial control volume C_i by taking the averaged density and linear momentum fields on the cell:

$$\int_{C_i} \rho^n \mathbf{g} dV = |C_i|\, \rho^n_i \mathbf{g}, \quad \int_{C_i} \mathbf{g} \cdot \mathbf{W}^n_{\mathbf{u}} dV = |C_i|\, \mathbf{g} \cdot \mathbf{W}^n_{\mathbf{u}\,i}. \tag{61}$$

3.2.5. Heat flux term

Let us assume that the averaged cell temperature Θ^n_i is known. Then, it can be used to approximate the temperature gradients on each primal cell as already done for the gradients of conservative variables in the flux and viscous terms. Finally, these values are employed to approximate the integral of the heat flux term after applying Gauss theorem,

$$\int_{C_i} \mathrm{div} \mathbf{Q}^n dV = \sum_{N_j \in \mathcal{K}_i} \mathbf{Q}^n_{T_{ij}} \cdot \boldsymbol{\eta}_{ij} = - \sum_{N_j \in \mathcal{K}_i} \lambda \left(\nabla\, \Theta^n\right)_{T_{ij}} \cdot \boldsymbol{\eta}_{ij} \tag{62}$$

From the implementation point of view, the temperature, Θ^n_i can be computed at the previous time step using the averaged values of the pressure and density at the dual cells:

$$\Theta^n_i = \frac{P^n_i}{\rho^n_i R}. \tag{63}$$

3.3. Pre-projection stage

Some of the terms in the pressure system require for the preprocessing of the involved variables since they need to be transferred from the dual mesh to the primal one, or they do not belong to the original unknowns of the system to be solved.

Given a scalar variable at the dual cells, W_i, its value on the primal element T_k is computed as the weighted average of the values on the subelements of a primal element associated to each face, T_{ki}, $i \in \mathcal{K}_k$, $\mathcal{K}_k$ the set of indexes identifying the faces of primal elements,

$$W_k = \sum_{i \in \mathcal{K}_k} W_i \frac{|T_{ki}|}{|T_k|}. \tag{64}$$

This approach is used for the computation of the density, W^{n+1}_ρ, the intermediate velocity, $\widetilde{\widetilde{\mathbf{W}}}_{\mathbf{u}}$, and the intermediate total energy density, $\widetilde{W}_E$, by primal element. Then, the first guess for the kinetic energy density,

$$(\rho K)^{n+1,1} = \frac{1}{2\rho^{n+1}} \left|\mathbf{W}^{n+1,1}_{\mathbf{u}}\right|^2, \tag{65}$$

is obtained. On the other hand, the first guess for the enthalpy is initially computed at the dual mesh,

$$H_i^{n+1,1} = \frac{\gamma}{\gamma-1}\frac{P_i^n}{\rho_i^{n+1}} \tag{66}$$

and used when its value on the faces of the primal elements is needed. Passing to a value per primal element is again done following (64).

3.4. Projection stage

For the projection stage a classical $\mathbb{P}_1$ continuous finite element method is employed to approximate the pressure correction $\delta P^{n+1,k+1}$ in the primal grid nodes in each Picard iteration. To get the weak formulation of the Laplacian problem we start by multiplying equation (28) by a test function $z \in V_0$, $V_0 := \left\{z \in H^1(\Omega) : \int_\Omega z dV = 0\right\}$, integrating in Ω and applying Green's formula:

$$\begin{aligned}
&\frac{1}{\gamma-1}\int_\Omega \delta P^{n+1,k+1} z \,\mathrm{dV} - \Delta t^2 \int_\Omega H^{n+1,k} \nabla \delta P^{n+1,k+1} \cdot \nabla z dV = \\
&\Delta t^2 \int_\Gamma H^{n+1,k} \nabla \delta P^{n+1,k+1} \cdot \boldsymbol{\eta} z dA + \int_\Omega \left(\widetilde{W}_E - (\rho K)^{n+1,k}\right) z dV \\
&-\frac{1}{\gamma-1}\int_\Omega P^n z dV + \Delta t \int_\Omega H^{n+1,k} \widetilde{\widetilde{\mathbf{W}}}_{\mathbf{u}} \cdot \nabla z dV - \Delta t \int_\Gamma H^{n+1,k} \widetilde{\widetilde{\mathbf{W}}}_{\mathbf{u}} \cdot \boldsymbol{\eta} z dA,
\end{aligned} \tag{67}$$

Next, taking into account (17), we have

$$\widetilde{\widetilde{\mathbf{W}}}_{\mathbf{u}} = \widetilde{\mathbf{W}}_{\mathbf{u}} - \Delta t \nabla P^n = \mathbf{W}_{\mathbf{u}}^{n+1} + \Delta t \nabla P^{n+1} = \mathbf{W}_{\mathbf{u}}^{n+1} + \Delta t \nabla \delta P^{n+1}. \tag{68}$$

Multiplication by the time step, Δt, the enthalpy, $H^{n+1,k}$, the normal vector, $\boldsymbol{\eta}$ and the test function, z, and integration in the boundary of the computational domain, Γ, gives

$$\Delta t \int_\Gamma H^{n+1,k} \widetilde{\widetilde{\mathbf{W}}}_{\mathbf{u}} \cdot \boldsymbol{\eta} z dA = \Delta t \int_\Gamma H^{n+1,k} \mathbf{W}_{\mathbf{u}}^{n+1} \cdot \boldsymbol{\eta} z dA + \Delta t^2 \int_\Gamma H^{n+1,k} \nabla \delta P^{n+1} \cdot \boldsymbol{\eta} z dA. \tag{69}$$

Rearranging the above equation, we get

$$\Delta t \int_\Gamma H^{n+1,k} \widetilde{\widetilde{\mathbf{W}}}_{\mathbf{u}} \cdot \boldsymbol{\eta} z dA - \Delta t^2 \int_\Gamma H^{n+1,k} \nabla \delta P^{n+1} \cdot \boldsymbol{\eta} z dA = \Delta t \int_\Gamma H^{n+1,k} \mathbf{W}_{\mathbf{u}}^{n+1} \cdot \boldsymbol{\eta} z dA. \tag{70}$$

Substitution of (70) into (67) leads to the following weak problem:

Weak problem. *In each Picard iteration k find the pressure correction $\delta P^{n+1,k+1} \in V_0$ that satisfies*

$$\begin{aligned}
&\frac{1}{\gamma-1}\int_\Omega \delta P^{n+1,k+1} z \,\mathrm{dV} - \Delta t^2 \int_\Omega H^{n+1,k} \nabla \delta P^{n+1,k+1} \cdot \nabla z \, dV = \\
&-\Delta t \int_\Gamma H^{n+1,k} \mathbf{W}_{\mathbf{u}}^{n+1} \cdot \boldsymbol{\eta} z dA + \int_\Omega \left(\widetilde{W}_E - (\rho K)^{n+1,k}\right) z dV - \frac{1}{\gamma-1}\int_\Omega P^n z dV + \Delta t \int_\Omega H^{n+1,k} \widetilde{\widetilde{\mathbf{W}}}_{\mathbf{u}} \cdot \nabla z dV,
\end{aligned} \tag{71}$$

for all $z \in V_0$.

The presence of the enthalpy and the kinetic energy on (71) would make the above system highly nonlinear if H^{n+1} and $(\rho K)^{n+1}$ would have been employed instead of $H^{n+1,k}$ and $(\rho K)^{n+1,k}$. To avoid direct resolution of such a complex system a classical approach consists in employing a Picard iteration procedure. Following the ideas introduced in [101, 102, 39, 64, 66] to circumvent the non-linearities arising in semi-implicit and locally implicit schemes for nonlinear PDEs, the enthalpy and the kinetic energy term on the right hand side of (71) are discretised at the previous Picard iteration, becoming thus explicit.

Consequently, at each Picard iteration, $k = 1, \ldots, N_{Pic}$, we have got a symmetric and positive definite system for the pressure correction that can be efficiently solved using classical numerical algorithms for linear systems like the conjugate gradient method using the solution at time t^n as initial guess for $k = 1$. Since in the numerical tests of this paper only the ideal gas equation of state has been considered, no mass lumping was applied. Let us also remark that for ODEs the Picard iteration procedure allows to gain one order in time per iteration so $N_{Pic} = 2$ might be enough to keep the accuracy of the developed scheme. Once (71) is solved, the solution is replaced into (30) to update the pressure and the enthalpy,

$$H^{n+1,k+1} = \frac{\gamma}{\gamma - 1} \frac{P^{n+1,k+1}}{\rho^{n+1}}, \tag{72}$$

and the density kinetic energy,

$$(\rho K)^{n+1,k+1} = \frac{1}{2\rho^{n+1}} \left| \mathbf{W}_{\mathbf{u}}^{n+1,k+1} \right|^2, \quad \mathbf{W}_{\mathbf{u}}^{n+1,k+1} = \widetilde{\widetilde{\mathbf{W}}}_{\mathbf{u}} - \Delta t \nabla \delta P^{n+1,k+1}, \tag{73}$$

can be computed to be used in the next Picard iteration.

3.5. Post-projection stage

Once the pressure P^{n+1} at the new time t^{n+1} and the new momentum $\mathbf{W}_{\mathbf{u}}^{n+1}$, are computed from (30) and (29), the total energy density must be updated. Integrating equation (31) on a spatial control volume T_k of the primal mesh and applying Gauss theorem yields

$$W_{E,k}^{n+1} = \widetilde{W}_{E,k} - \frac{\Delta t}{|T_k|} \sum_{N_l \in \mathcal{K}_k} \int_{\Gamma_{kl}} H^{n+1} \mathbf{W}_{\mathbf{u}}^{n+1} \cdot \tilde{\boldsymbol{\eta}}_{kl} dS. \tag{74}$$

where $\tilde{\boldsymbol{\eta}}_{kl}$ denotes the unit normal vector to the l-face Γ_{kl} of the primal element T_k. To approximate the integral on the face we assume a constant value for the linear momentum given by its averaged value on the dual cell C_i containing the face Γ_{kl}. Regarding the enthalpy, the averaged value of the vertex of the face is employed. The averaged total energy density at each primal element is then interpolated into the dual mesh using a weighted average,

$$W_{E,i}^{n+1} = \frac{1}{|C_i|} \sum_{N_k \in \mathcal{K}_i} |T_{ki}| \, W_{E,k}^{n+1}, \tag{75}$$

with $|T_{ki}|$ the area/volume of the intersection between the primal element T_k and the dual element C_i.

Remark 3.1. *An alternative to update the total energy density would consist on computing on the primal grid only the contribution of the last term of* (74)*. Then, it can be interpolated to the dual grid and added to the intermediate value* $\widetilde{W}_E$ *originally computed on the dual grid. This approach would reduce dissipation arising from forward-backward interpolation between meshes.*

3.6. Boundary conditions

Boundary conditions of the numerical tests to be presented in Section 4 are constructed as a combination of:

- *Periodic* boundary conditions. For the implementation of periodic boundary conditions, we assume that a periodic mesh is provided. The pairs of matching dual boundary elements are combined in order to define a new dual cell which then becomes of the interior type. Concerning the finite element method, the corresponding vertexes are merged, resulting in a reduced number of unknowns for the pressure system. All connections between the elements and nodes need to be updated accordingly.

- *Strong Dirichlet* boundary conditions on FV. The exact value at the boundary is imposed as the averaged value on the cell. Let us note that for inviscid flows only the normal component is set. When adiabatic walls are selected, we impose zero heat flux instead of defining the value of the density field. Definition of the exact value of the linear momentum is conveyed to the pressure system where it is used to compute the last term in equation (71).

- *Weak Dirichlet* boundary conditions on FV. The value of a variable on the boundary is employed to compute the contribution of the different terms of the corresponding conservative equations on boundary cells. Accordingly, the computation of gradients with the Galerkin approach makes use of the exact value of the variable at the boundary node whereas the numerical flux is computed considering an auxiliary state:

$$\mathbf{W}^{\mathbf{u}}_{\text{aux}} = 2\mathbf{W}^{\mathbf{u}}_{\text{exact}} - \mathbf{W}^{\mathbf{u}}_{i} \tag{76}$$

  in the viscous case and

$$\mathbf{W}^{\mathbf{u}}_{\text{aux}} = \mathbf{W}^{\mathbf{u}}_{i} - 2\mathbf{W}^{\mathbf{u}}_{i} \cdot \widetilde{\boldsymbol{\eta}}\widetilde{\boldsymbol{\eta}} \tag{77}$$

  for inviscid wall boundary conditions. Likewise strong Dirichlet boundary conditions, they are usually combined with Neumann boundary conditions for the pressure field.

- Neumann boundary conditions on FV. They are generally linked to Dirichlet boundary conditions on the pressure system so the exact value is imposed on boundary vertex. No further computations are needed for the definition of inflow and outflow conditions on the velocity field.

4. Numerical results

The developed methodology is assessed using classical benchmarks from the incompressible limit to high Mach number flows. For all tests presented in the following, we consider SI units. The time step is determined according to the condition

$$\Delta t = \min_{C_i} \{\Delta t_i\}, \qquad \Delta t_i = \text{CFL} \frac{r_i^2}{(|\zeta|_{\max} + c_\alpha) r_i + 2\left[\frac{4}{3}\left(|\nu|_{\max} + \frac{\gamma\lambda}{c_p\rho}\right)\right]} \tag{78}$$

where $|\zeta|_{\max}$, $|\nu|_{\max}$ and λ denote the maximum absolute eigenvalues related to the convective and diffusive terms, respectively, which have been discretized explicitly, and c_α is an artificial viscosity parameter, which in this paper is assumed to be constant in space and time for simplicity. If not explicitly stated otherwise, $c_\alpha = 0$ is used as default value. In (78), the symbol r_i denotes the incircle diameter of each dual control volume. The default value for the CFL number for all test cases is CFL$= 1/d$, with d the number of space dimensions. Besides, the CFL related to the sound speed, CFL$_c$, indicated in the tests is computed as

$$\text{CFL}_c = \max_{C_i} \left(c_i \frac{\Delta t}{r_i}\right), \quad c_i = \sqrt{\gamma \frac{P_i}{\rho_i}}. \tag{79}$$

In the rest of this section, gravity is neglected, hence the gravity vector is set to $\mathbf{g} = \mathbf{0}$.

4.1. Taylor-Green vortex and numerical convergence results

To study the accuracy of the new method proposed in this paper the Taylor-Green vortex problem is solved in 2D. We consider a computational domain $\Omega = [0, 2\pi] \times [0, 2\pi]$ discretized using the meshes described in Table 1 and a final simulation time $t_{\text{end}} = 0.1$. The exact solution for this test case reads

$$\rho(\mathbf{x}, t) = 1, \quad \mathbf{u}(\mathbf{x}, t) = \begin{pmatrix} \sin(x)\cos(y) \\ -\cos(x)\sin(y) \end{pmatrix}, \quad p(\mathbf{x}, t) = \frac{p_0}{\gamma - 1} + \frac{1}{4}(\cos(2x) + \cos(2y)), \tag{80}$$

Mesh	Elements	Vertices	Dual elements
M_1	512	289	800
M_2	2048	1089	3136
M_3	8192	4225	12416
M_4	32768	16641	49408
M_5	131072	66049	197120
M_6	524288	263169	787456

Table 1: Different meshes used for the numerical convergence study based on the Taylor-Green vortex.

with $\gamma = 1.4$, $p_0 = 10^5$. This leads to a characteristic Mach number $M \approx 1.7 \cdot 10^{-3}$, so it corresponds to the low Mach number regime. In this particular test case, the time step has not been automatically computed from the CFL condition, instead a fixed value starting from $\Delta t = 0.25$ for the coarsest mesh and decreasing linearly according to the mesh size has been employed. The L^2 errors in space, computed at the final time step, and the order of accuracy attained,

$$L^2_{\Omega,\,M_i}(W) = \|W_{\text{exact}} - W_{M_i}\|_{L^2(\Omega)}\,, \quad \mathcal{O}_{M_i/M_j}(W) = \frac{\log\left(L^2_{\Omega,\,M_i}(W)/L^2_{\Omega,\,M_j}(W)\right)}{\log\left(h_{M_i}/h_{M_j}\right)}, \tag{81}$$

are depicted in Table 2. The sought order of accuracy is reached for the main flow variables with both the first order and LADER schemes, as for the hybrid FV/FE scheme for the incompressible Navier-Stokes equations proposed in [1]. At this point, we would like to remark that the proposed scheme is nominally only first order accurate in time due to the employed operator splitting technique. In order to achieve high order also in time, we recommend the use of an IMEX Runge-Kutta scheme, see e.g. [103, 40, 41, 44, 45, 46].

Mesh	$L^2_\Omega(\rho)$	$\mathcal{O}(\rho)$	$L^2_\Omega(\mathbf{u})$	$\mathcal{O}(\mathbf{u})$	$L^2_\Omega(E)$	$\mathcal{O}(E)$	$L^2_\Omega(p)$	$\mathcal{O}(p)$
First order scheme								
M1	$1.51E{-}01$		$2.23E{-}01$		$1.74E{+}03$		$2.77E{-}01$	
M2	$8.19E{-}02$	0.88	$1.13E{-}01$	0.98	$3.74E{+}02$	2.22	$5.47E{-}02$	2.34
M3	$4.12E{-}02$	0.99	$5.66E{-}02$	0.99	$8.71E{+}01$	2.10	$2.95E{-}02$	0.89
M4	$2.06E{-}02$	1.00	$2.84E{-}02$	1.00	$2.13E{+}01$	2.03	$1.55E{-}02$	0.93
M5	$1.03E{-}02$	1.00	$1.42E{-}02$	1.00	$5.28E{+}00$	2.01	$7.96E{-}03$	0.96
M6	$5.14E{-}03$	1.00	$7.11E{-}03$	1.00	$1.32E{+}00$	2.00	$4.03E{-}03$	0.98
LADER scheme								
M1	$4.23E{-}03$		$3.06E{-}02$		$7.20E{+}01$		$1.10E{-}01$	
M2	$9.71E{-}04$	2.12	$7.69E{-}03$	1.99	$3.82E{+}00$	4.24	$2.99E{-}02$	1.87
M3	$2.37E{-}04$	2.04	$1.92E{-}03$	2.00	$2.29E{-}01$	4.06	$7.56E{-}03$	1.98
M4	$5.84E{-}05$	2.02	$4.78E{-}04$	2.00	$1.50E{-}02$	3.93	$1.90E{-}03$	1.99
M5	$1.45E{-}05$	2.01	$1.19E{-}04$	2.00	$1.21E{-}03$	3.64	$4.76E{-}04$	2.00
M6	$3.60E{-}06$	2.01	$2.99E{-}05$	2.00	$1.63E{-}04$	2.89	$1.19E{-}04$	2.00

Table 2: Taylor-Green vortex. Spatial L_2 error norms obtained at time $t_{\text{end}} = 0.1$, and convergence rates for the first order and local ADER schemes.

4.2. Riemann problems

In this section, we analyse the performance of the proposed methodology for the compressible Euler equations in presence of medium to strong shocks. We consider a two-dimensional computational domain with $x \in [-0.5, 0.5]$ and a variable width depending on the number of cells in the horizontal direction so that the final elements have a good aspect ratio and a small number of layers in the y-direction to reduce the computational cost of the simulation. The initial condition is defined as

$$\rho^0(\mathbf{x}) = \begin{cases} \rho_L & \text{if } x \leq x_c, \\ \rho_R & \text{if } x > x_c; \end{cases} \qquad u_1^0(\mathbf{x}) = \begin{cases} u_L & \text{if } x \leq x_c, \\ u_R & \text{if } x > x_c; \end{cases} \qquad u_2^0(\mathbf{x}) = 0 \qquad p^0(\mathbf{x}) = \begin{cases} p_L & \text{if } x \leq x_c, \\ p_R & \text{if } x > x_c; \end{cases} \tag{82}$$

where ρ_L, ρ_R, p_L, p_R, u_L, u_R, x_c are summarized in Table 3 for the diverse tests, selected among those presented in [29, 66]. The final time of each simulation, as well as the number of mesh divisions along the x-axis (N_x), have also been reported in Table 3. The characteristic mesh spacing is therefore equal to $h = 1/N_x$. All tests have been run with the first order and LADER schemes using Dirichlet boundary conditions in the x-direction and periodic boundary conditions in the y-direction. The first test analysed,

Test	ρ_L	ρ_R	u_L	u_R	p_L	p_R	x_c	t_{end}	N_x
RP1	1	0.125	0	0	1	0.1	0	0.2	200
RP2	1	1	-1	1	0.4	0.4	0	0.15	300
RP3	0.445	0.5	0.698	0	3.528	0.571	0	0.14	200
RP4	5.99924	5.99242	19.5975	-6.19633	460.894	46.095	-0.2	0.035	200
RP5	1	1	-19.59745	-19.59745	1000.0	0.01	0.3	0.01	300
RP6	1	1	2	-2	0.1	0.1	0	0.8	200

Table 3: Riemann problems. Initial condition, initial position of the discontinuity, x_c, final time, t_{end}, and number of mesh cells on x-direction, N_x, for each Riemann problem.

RP1, is the classical Sod problem presented for the first time in [104]. Figure 3 shows a good agreement between the numerical and the exact solution for the shock, the contact, and the rarefaction waves.

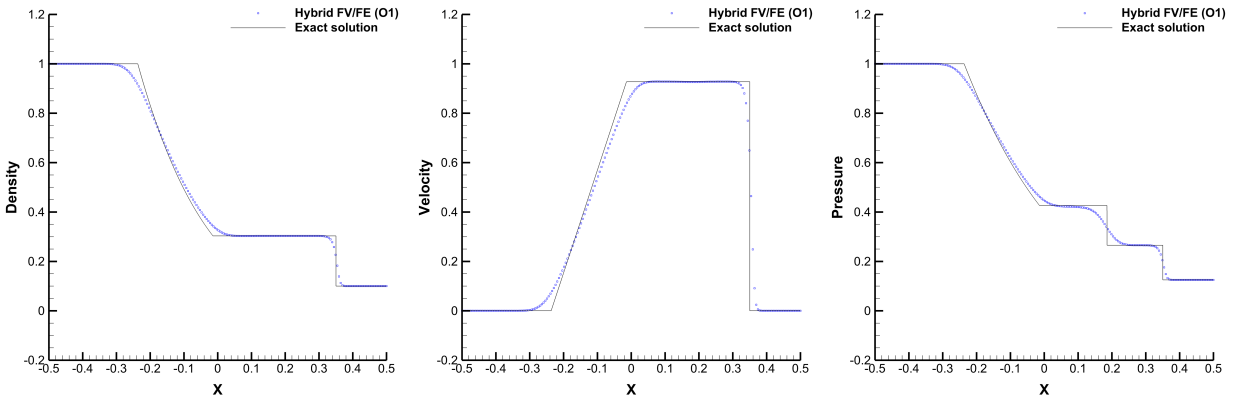

Figure 3: Riemann problem 1 (Sod). 1D cut through the numerical results along the line $y = 0$ for ρ, u and p at $t_{\text{end}} = 0.2$ using the first order method ($\text{CFL}_c = 3.35$, $c_\alpha = 1$, $M \approx 0.93$).

RP2 corresponds to a double rarefaction problem. Overall the shape of the exact solution is captured even if a finer mesh would be useful to better approximate the constant contact discontinuity between the two rarefactions, Figures 5-6.

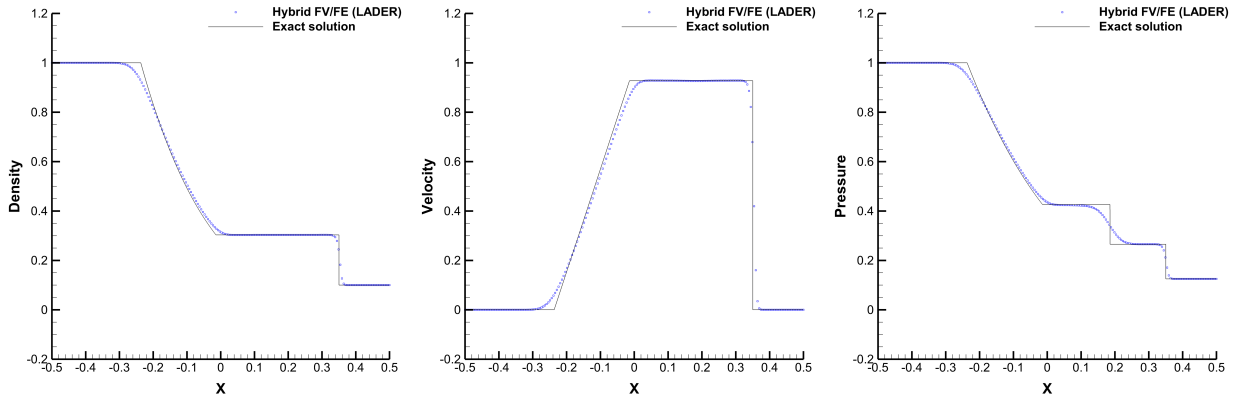

Figure 4: Riemann problem 1 (Sod). 1D cut through the numerical results along the line $y = 0$ for ρ, u and p at $t_{\text{end}} = 0.2$ using the LADER-ENO method ($\text{CFL}_c = 3.35$, $c_\alpha = 1$, $M \approx 0.93$).

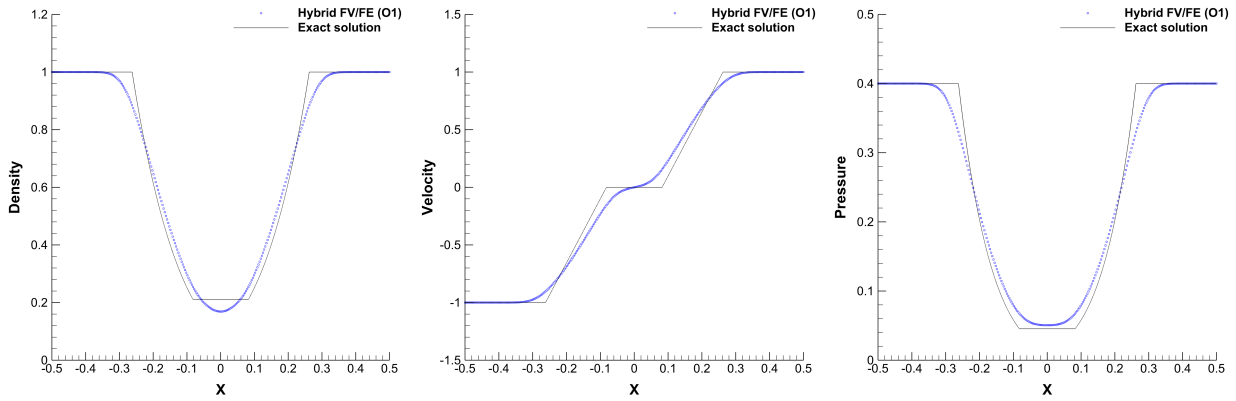

Figure 5: Riemann problem 2 (Double rarefaction). 1D cut through the numerical results along the line $y = 0$ for ρ, u and p at $t_{\text{end}} = 0.15$ using the first order method ($\text{CFL}_c = 0.4$, $c_\alpha = 2$, $M \approx 1.37$).

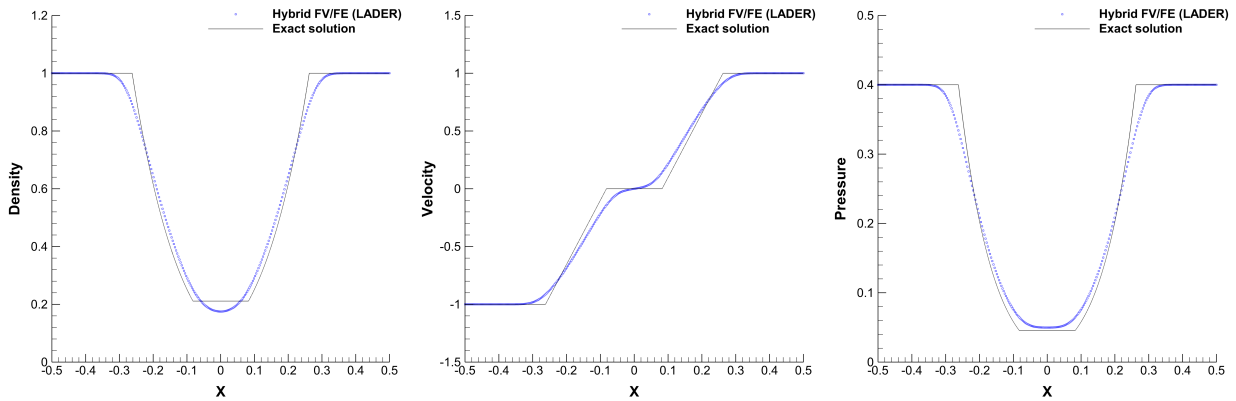

Figure 6: Riemann problem 2 (Double rarefaction). 1D cut through the numerical results along the line $y = 0$ for ρ, u and p at $t_{\text{end}} = 0.15$ using the LADER-ENO method ($\text{CFL}_c = 0.4$, $c_\alpha = 2$, $M \approx 1.37$).

The third test, RP3, corresponds to the Lax shock tube and is used to assess the ability of the method to deal with simple waves. The obtained results, presented in Figures 7-8, match pretty well the exact reference solution.

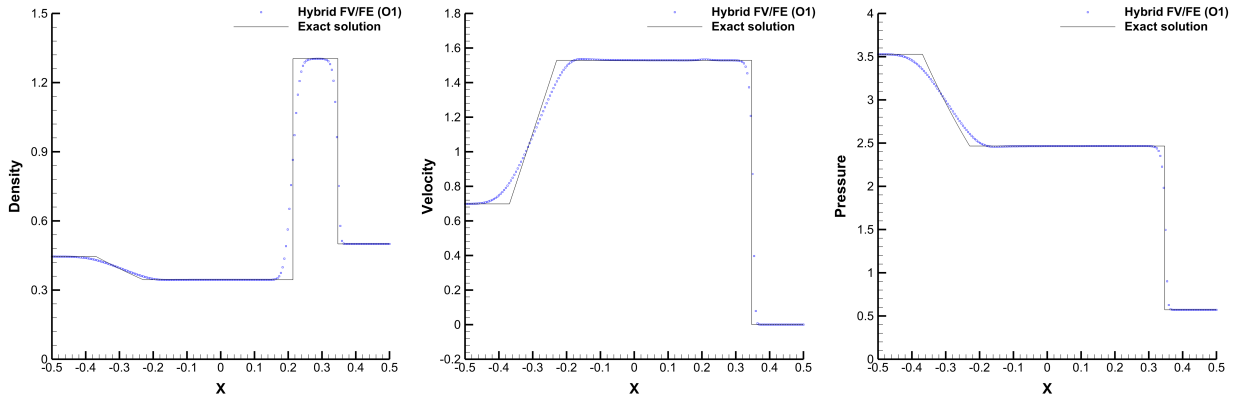

Figure 7: Riemann problem 3 (Lax). 1D cut through the numerical results along the line $y = 0$ for ρ, u and p at $t_{\text{end}} = 0.14$ using the first order method on mesh M1 ($\text{CFL}_c = 2.78$, $M \approx 0.94$).

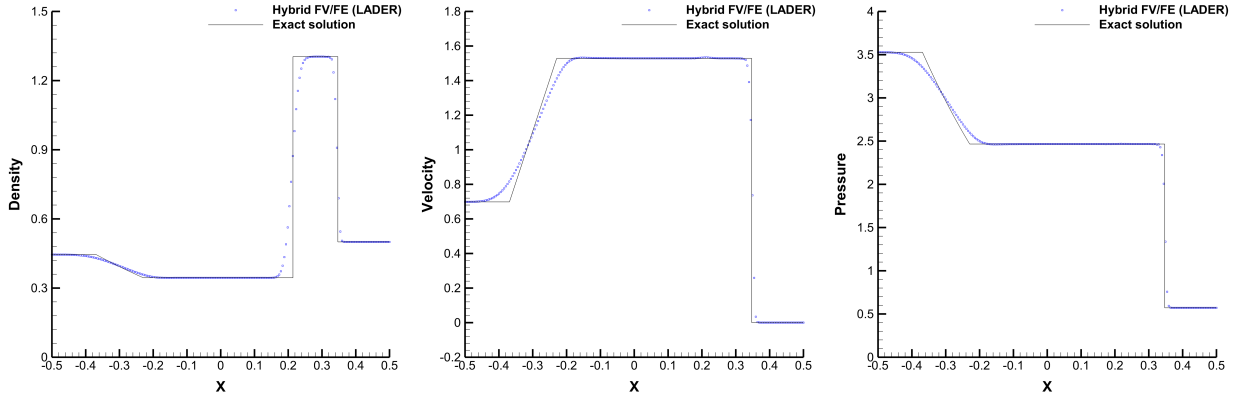

Figure 8: Riemann problem 3 (Lax). 1D cut through the numerical results along the line $y = 0$ for ρ, u and p at $t_{\text{end}} = 0.14$ using the LADER-ENO method on mesh M1 ($\text{CFL}_c = 2.78$, $M \approx 0.94$).

The fourth Riemann problem, RP4, presents three strong discontinuities travelling to the right originated from two shock colliding waves. Figures 9-10 show the solution obtained with the first and second order schemes. Note that the highly restrictive Barth and Jespersen limiter has been employed jointly with an artificial viscosity coefficient, $c_\alpha = 5$, to keep the stability of the scheme.

RP5 is a severe test defined as a modification of the left half of the blast problem introduced in [105]. It accounts for a left rarefaction wave, a right-travelling shock wave and a stationary contact discontinuity generated by an initial large pressure jump of order 10^5 and a small velocity variation. The second order scheme has been run using two different limiter strategies. We observe that the minmod limiter, Figure 13, is more severe on damping the oscillation appearing after the rarefaction wave on the velocity field than the ENO-based reconstruction, Figure 12, which captures better the right shock. The results obtained with the first order scheme are reported in Figure 11. The robustness of the developed methodology and its capability to deal with slowly moving contact discontinuities, for really high Mach numbers, are clearly proven.

The last Riemann problem considered, RP6, is characterised by two shock waves travelling in opposite directions. An excellent agreement with the exact solution is observed in Figures 14-15.

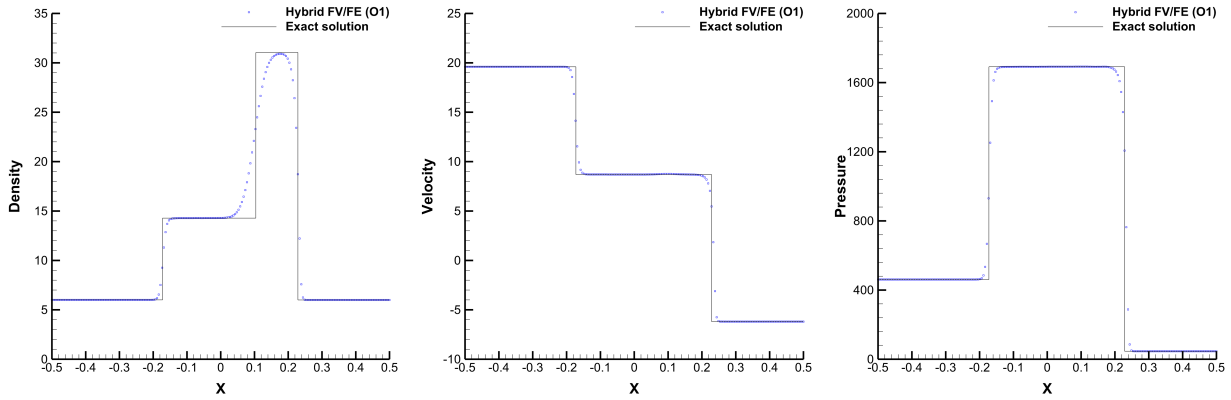

Figure 9: Riemann problem 4. 1D cut through the numerical results along the line $y = 0$ for ρ, u and p at $t_{\text{end}} = 0.035$ using the first order method ($\text{CFL}_c = 0.42$, $c_\alpha = 5$, $M \approx 1.97$).

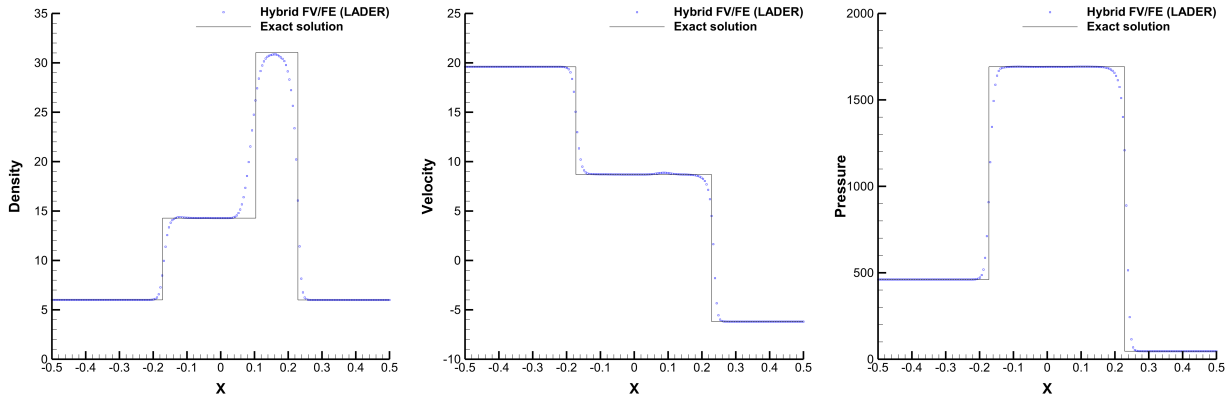

Figure 10: Riemann problem 4. 1D cut through the numerical results along the line $y = 0$ for ρ, u and p at $t_{\text{end}} = 0.035$ using LADER-BJ method with reconstruction thorough primitive variables instead the conservative ones ($\text{CFL}_c = 0.42$, $c_\alpha = 5$, $M \approx 1.97$).

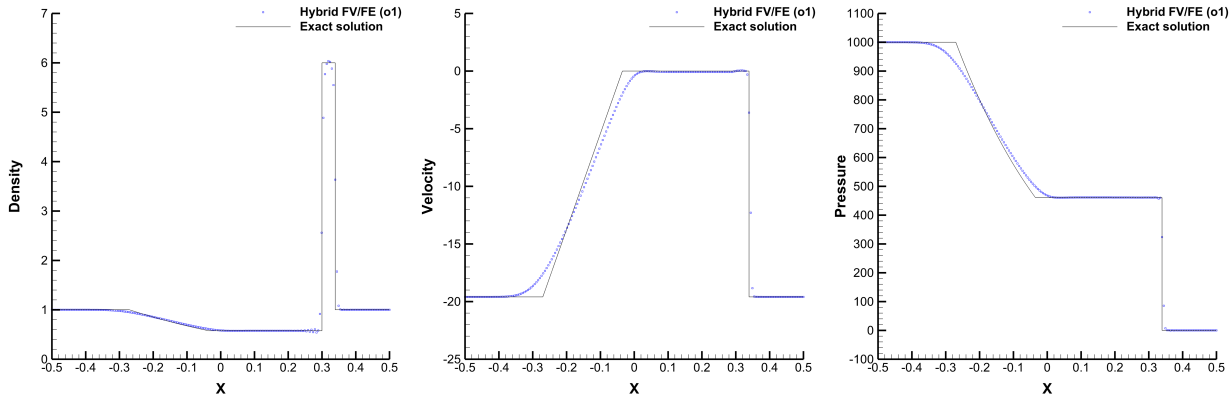

Figure 11: Riemann problem 5. 1D cut through the numerical results along the line $y = 0$ for ρ, u and p at $t_{\text{end}} = 0.01$ using the first order scheme ($\text{CFL}_c = 2.7 \cdot 10^{-3}$, $c_\alpha = 2$, $M \approx 956.42$).

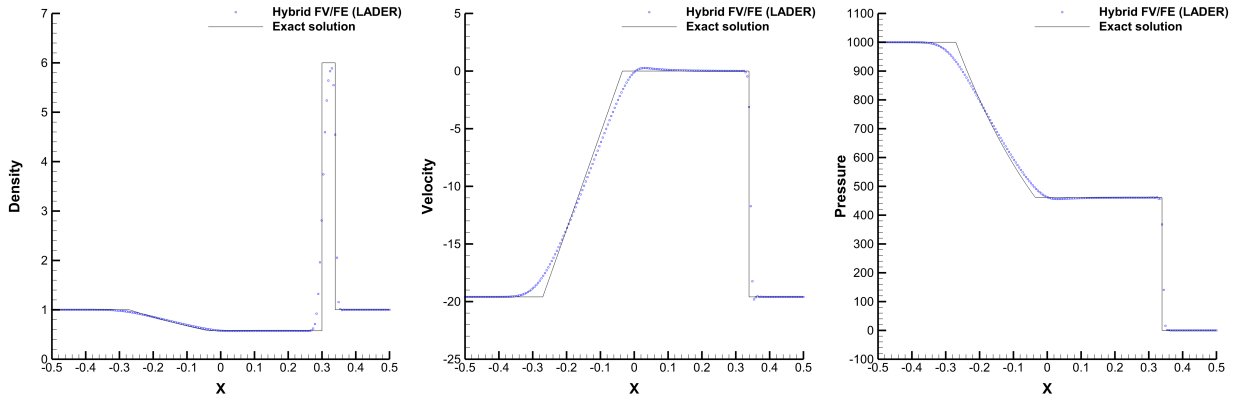

Figure 12: Riemann problem 5.1D cut through the numerical results along the line $y = 0$ for ρ, u and p at $t_{\text{end}} = 0.01$ using the LADER-ENO method ($\text{CFL}_c = 2.7 \cdot 10^{-3}$, $c_\alpha = 2$, $M \approx 513.68$).

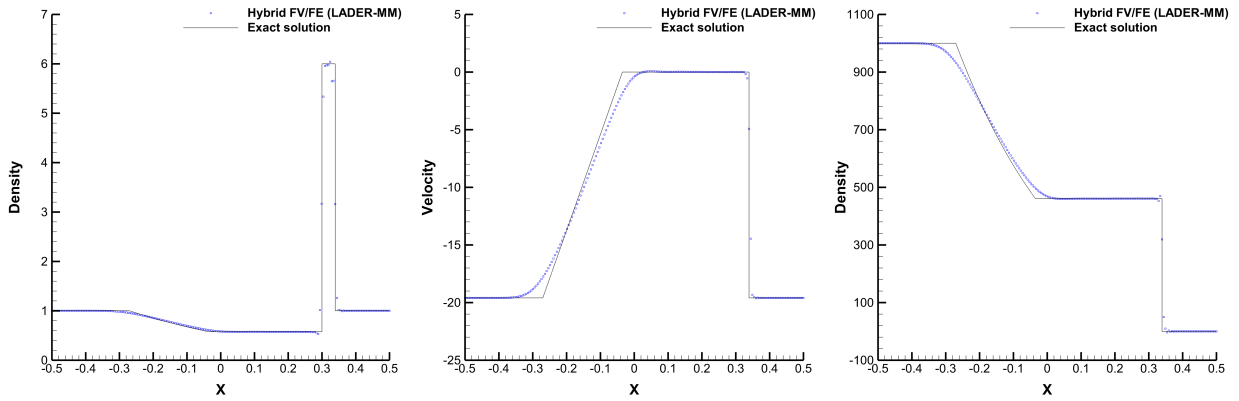

Figure 13: Riemann problem 5. 1D cut through the numerical results along the line $y = 0$ for ρ, u and p at $t_{\text{end}} = 0.01$ using the LADER-minmod method ($\text{CFL}_c = 2.7 \cdot 10^{-3}$, $c_\alpha = 2$, $M \approx 691.58$).

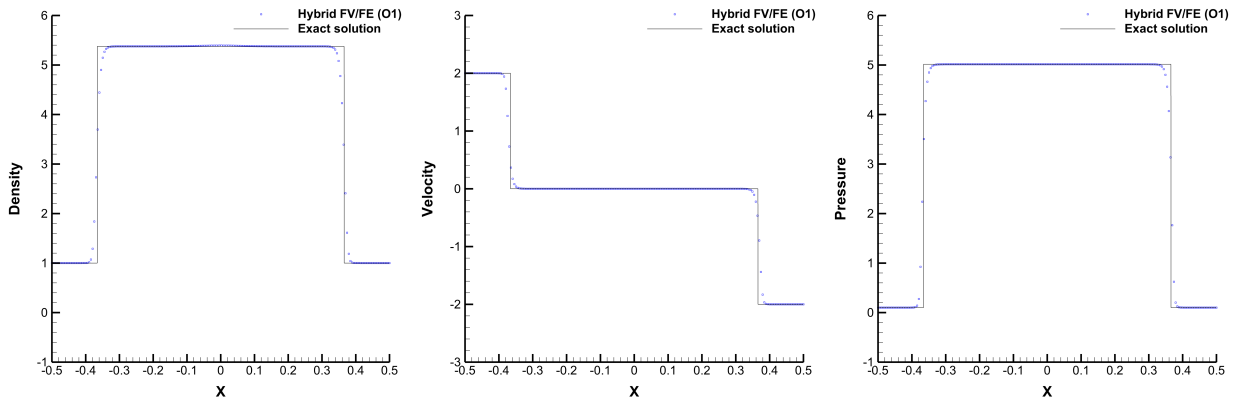

Figure 14: Riemann problem 6. 1D cut through the numerical results along the line $y = 0$ for ρ, u and p at $t_{\text{end}} = 0.8$ using the first order method ($\text{CFL}_c = 9.35$, $c_\alpha = 2$, $M \approx 7.75$).

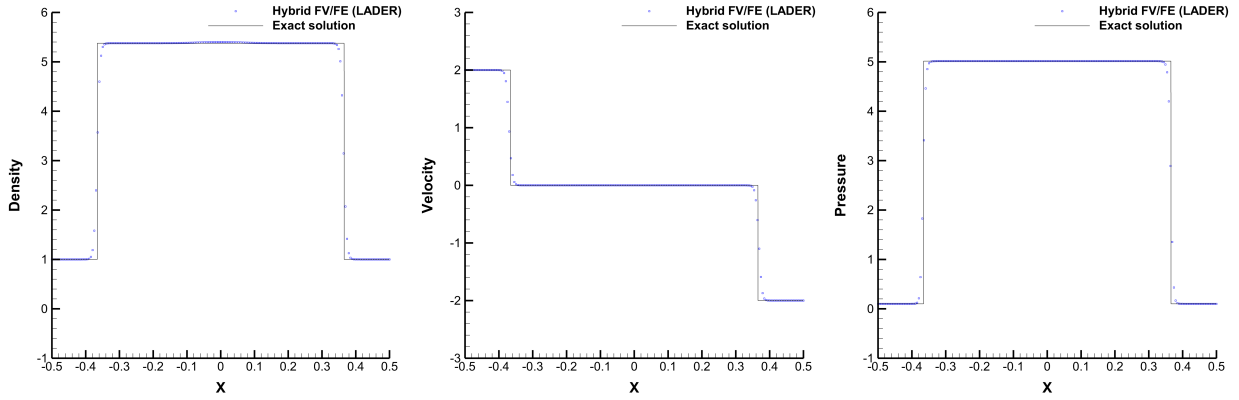

Figure 15: Riemann problem 6. 1D cut through the numerical results along the line $y = 0$ for ρ, u and p at $t_{\text{end}} = 0.8$ using the first order method ($\text{CFL}_c = 9.35$, $c_\alpha = 2$, $M \approx 7.29$).

4.3. 2D circular explosion

The circular explosion problem presented here is based on an initial radial solution given by the Sod shock tube

$$\rho^0(\mathbf{x}) = \begin{cases} 1 & \text{if } r \leq 0.5, \\ 0.125 & \text{if } r > 0.5, \end{cases} \qquad \mathbf{u}^0(\mathbf{x}) = 0, \qquad p^0(\mathbf{x}) = \begin{cases} 1 & \text{if } r \leq 0.5, \\ 0.1 & \text{if } r > 0.5, \end{cases} \tag{83}$$

see [29, 106, 71]. We consider the computational domain $\Omega = [-1, 1] \times [-1, 1]$ and periodic boundary conditions everywhere. The simulation is run until time $t_{\text{end}} = 0.25$ on a primal triangular mesh of 85344 elements. To get a reference solution, a one-dimensional PDE in the radial direction obtained from the compressible Euler equations when using convenient geometrical source terms, [29], is solved using a second order TVD scheme on a very fine mesh made of 10000 elements. The results obtained with the first order scheme and the LADER-ENO methodology, Figures 16-17, present a good agreement with the reference solution. Figure 18 allows for a direct comparison of the solution obtained with both schemes along a 1D cut. The second order LADER method with ENO reconstruction provides a better approximation of the solution compared to the first order scheme, as expected.

4.4. 3D spherical explosion

In this section, we study the behaviour of the method for a 3D spherical explosion benchmark based on the Sod problem. The computational domain is defined to be the sphere of unit radius centered at the origin. Initial conditions read

$$\rho^0(\mathbf{x}) = \begin{cases} 1 & \text{if } r \leq \frac{1}{2}, \\ 0.125 & \text{if } r > \frac{1}{2}, \end{cases} \qquad p^0(\mathbf{x}) = \begin{cases} 1 & \text{if } r \leq \frac{1}{2}, \\ 0.1 & \text{if } r > \frac{1}{2}, \end{cases} \qquad \mathbf{u}^0(\mathbf{x}) = 0, \tag{84}$$

with $r = \sqrt{x^2 + y^2 + z^2}$. Dirichlet boundary conditions are imposed and the domain is covered by 2280182 tetrahedra.

The solution obtained using the LADER-ENO scheme with CFL $= 1$, $c_\alpha = 3$, up to $t_{\text{end}} = 0.25$ is depicted in Figure 19. As reference solution we solve again the 1D code for Euler equations introduced in Section 4.3 updated with appropriate source terms to account for three-dimensional effects. The agreement observed for the 1D cuts of density, velocity magnitude and pressure prove the capability of the method to handle three-dimensional problems.

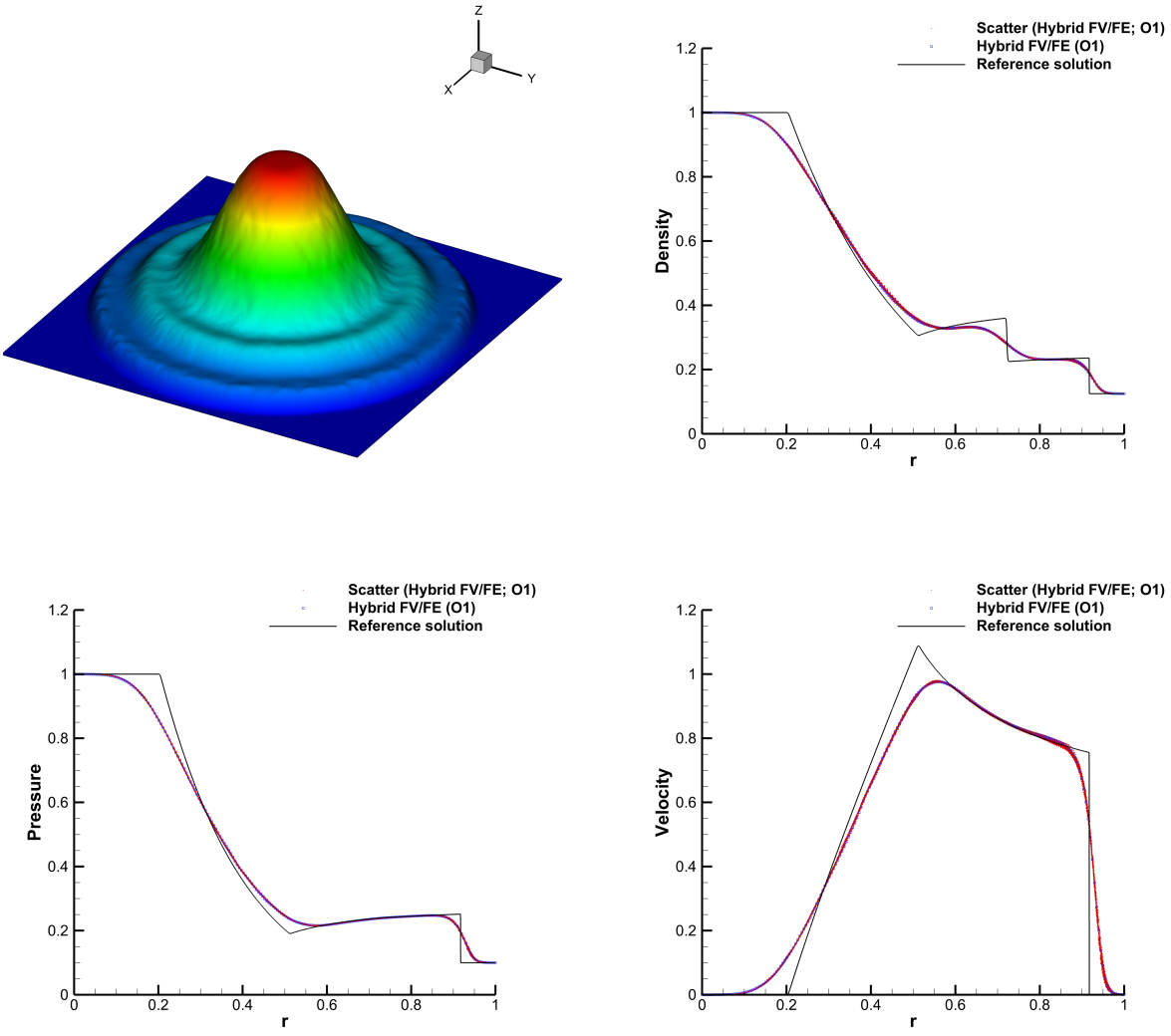

Figure 16: Circular explosion. The left top image corresponds to the 3D plot of the obtained ρ at the final time whereas the 1D plots containing the reference solution (black continuous line), a 1D cut (blue squared line) and the scatter plot (red dots), correspond to the ρ, p, and $|\mathbf{u}|$ fields obtained using the first order scheme ($c_\alpha = 1$).

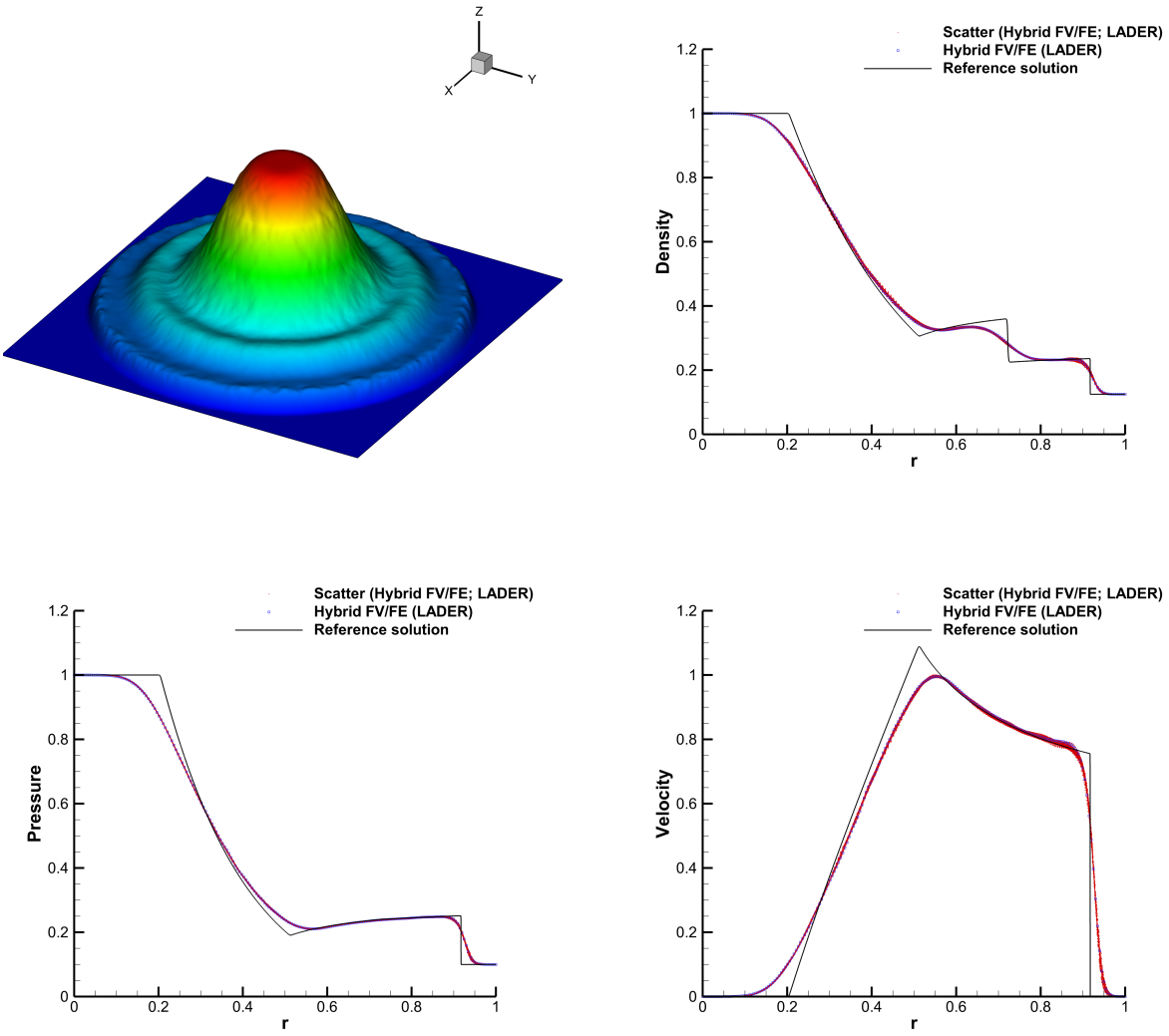

Figure 17: Circular explosion. The left top image corresponds to the 3D plot of the obtained ρ at the final time whereas the 1D plots containing the reference solution (black continuous line), a 1D cut (blue squared line) and the scatter plot (red dots), correspond to the ρ, p, and $|\mathbf{u}|$ fields obtained using the LADER-ENO scheme ($c_\alpha = 1$).

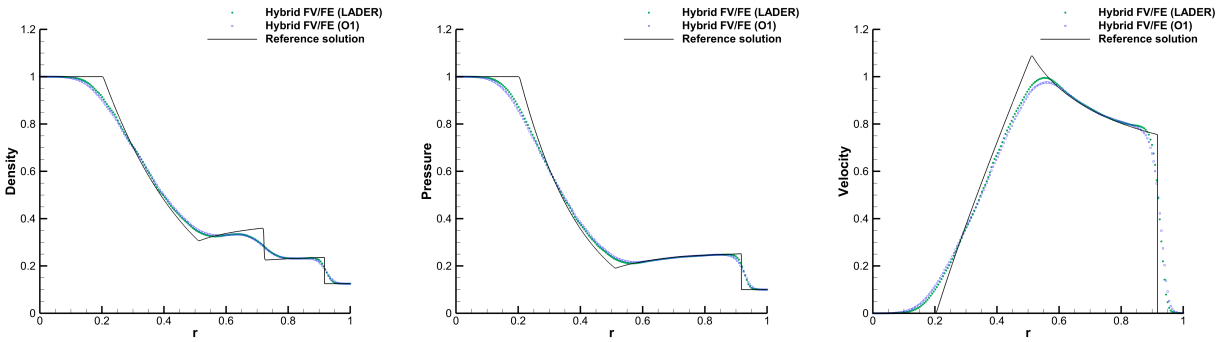

Figure 18: Circular explosion. Comparison between the numerical solution obtained with the first order scheme (blue squares) and the LADER-ENO approximation (green circles).

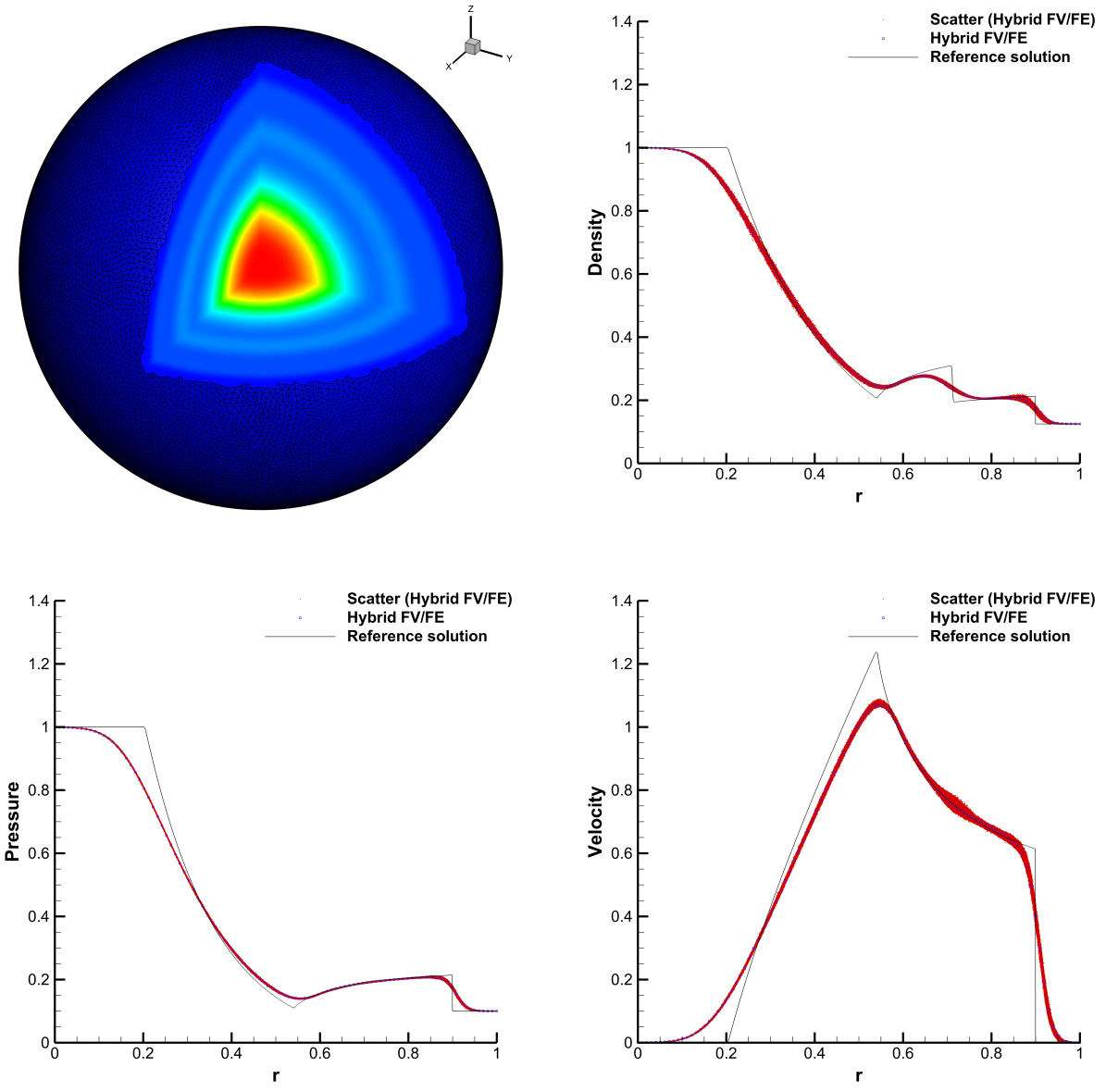

Figure 19: LADER-ENO solution for the 3D spherical explosion test at final time. Surface mesh on the boundary and density contours on the interior surfaces obtained after taking away the first quadrant and 1D plots for density, velocity magnitude and pressure fields: 1D cut on $x \in [0, 1]$, $y = z = 0$ (blue squares), scatter plot (red dots), reference solution (black line).

4.5. First problem of Stokes

To further analyse the behaviour of the developed method in the incompressible limit, we now consider the first problem of Stokes, [107]. The initial condition, defined in $\Omega = [-0.5, 0.5] \times [-0.5, 0.5]$, reads

$$\rho^0(\mathbf{x}) = 1, \qquad p^0(\mathbf{x}) = \frac{1}{\gamma}, \qquad u_1^0(\mathbf{x}) = 0, \qquad u_2^0(\mathbf{x}) = \begin{cases} -0.1 & \text{if } y \leq 0, \\ 0.1 & \text{if } y > 0 \end{cases} \tag{85}$$

In the incompressible limit, this test case has an exact analytical solution for u_2 given by

$$u_2(\mathbf{x}, t) = \frac{1}{10}\text{erf}\left(\frac{x}{2\sqrt{\mu t}}\right). \tag{86}$$

To complete the physical set up, we define $\gamma = c_p = 1.4$, $\lambda = 0$, leading to $M \approx 10^{-1}$. Regarding boundary conditions, we impose the exact values for density and velocity in the x-direction, while on the top and bottom boundaries, we set periodic boundary conditions in y-direction. Meanwhile, the exact values for density and velocity are employed in the remaining boundaries. Finally, three different simulations are run attending to the value for the viscosity coefficient: $\mu = 10^{-2}$, $\mu = 10^{-3}$, and $\mu = 10^{-4}$. The simulations are run on a triangular primal mesh made of 1000 elements up to time $t_{\text{end}} = 1$. The vertical velocity along $y = 0$ is plotted in Figure 20 against the exact solution. We observe a good agreement between both curves for all three viscosities. Let us note that $\mu = 10^{-4}$ is the only simulation run using the ENO reconstruction so that we completely avoid the small bump arising after the discontinuity if any limiting strategy is employed. In the other cases, such reconstruction can be neglected due to the high physical viscosity considered.

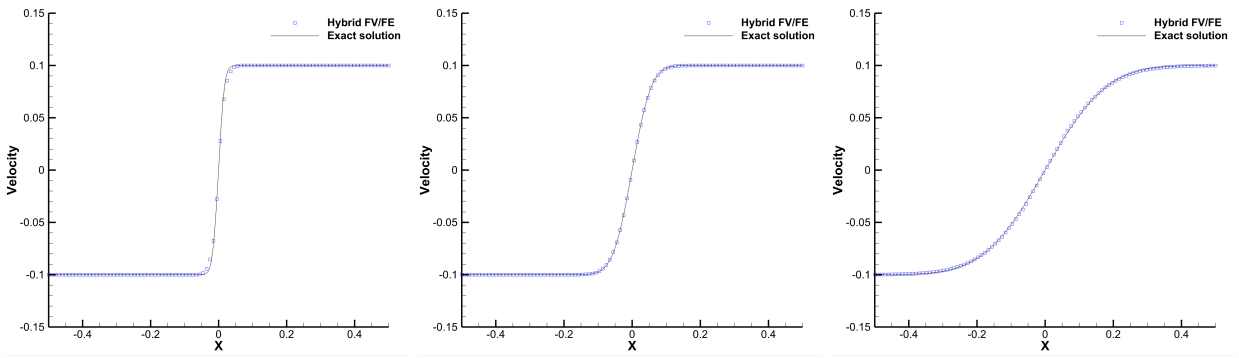

Figure 20: Comparison of the vertical velocity u_2 along the 1D cut $y = 0$ obtained for the first Stokes problem using LADER scheme against the exact solution at $t_{\text{end}} = 1$. $\mu = 10^{-4}$ LADER-EN (left), $\mu = 10^{-3}$ LADER without limiters (center), $\mu = 10^{-2}$ LADER without limiters (right).

4.6. Viscous shock

Here we analyse a steady viscous shock with $M_s = 2$ the shock Mach number. Considering the particular case Pr= 0.75, with Pr the Prandtl number, it is possible to find an exact solution of the compressible Navier-Stokes equations, derived by Becker in 1923, see [108, 109, 110] for all the necessary details to setup this test case.

The computational domain $\Omega = [-0.5, 0.5] \times [0, 0.1]$ is discretized with 12500 triangular elements of characteristic mesh spacing $h = 1/250$. The shock wave is centered at $x = 0$.

The values of the fluid in front of the shock wave are given by $\rho_0 = 1$, $u_0 = -2$, $v_0 = w_0 = 0$, and $p_0 = 1/\gamma$ so that the corresponding sound speed is $c_0 = 1$ and the fluid is moving into the shock from the right to the left at shock Mach number $M_s = 2$. The Reynolds number based on a unitary reference length ($L = 1$) and on the flow speed u_0 is given by $Re_s = \frac{\rho_0 c_0 M_s L}{\mu}$. The fluid parameters are chosen as $\gamma = 1.4$, $c_v = 2.5$, $\mu = 2 \cdot 10^{-2}$ and $\lambda = 9\frac{1}{3} \cdot 10^{-2}$, hence the corresponding shock Reynolds number is $Re_s = 100$. The simulation with the new hybrid FV/FE scheme proposed in this paper is run until time $t_{\text{end}} = 0.025$, setting $c_\alpha = 3$. The comparison between the numerical solution and the exact solution is shown in Figure 21 for the density ρ, the velocity u, and the pressure p. For all quantities, one can note a very good agreement.

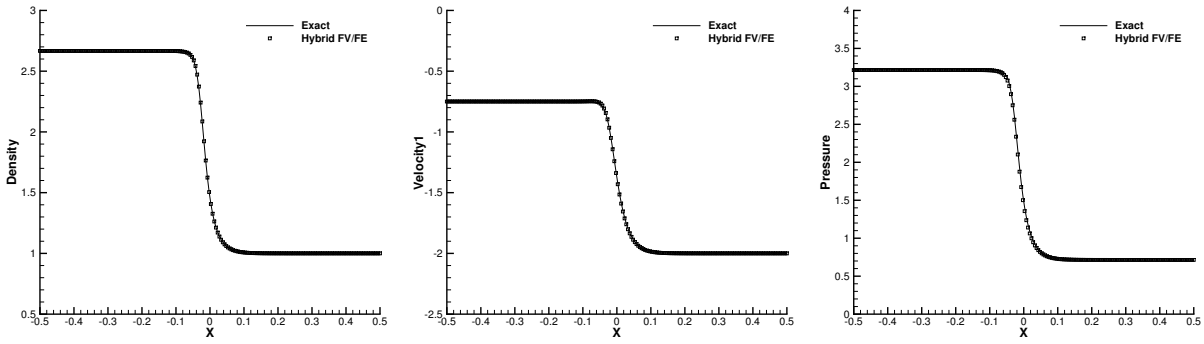

Figure 21: Numerical solution for the steady viscous shock obtained with the hybrid FV/FE scheme and exact solution of the compressible Navier-Stokes equations, Pr= 0.75, $M = 2$ and $Re = 100$ at time $t = 0.025$.

4.7. Lid-driven cavity flow

A classical test for incompressible flows is the lid-driven cavity benchmark, which accounts for a well-known reference solution, [111]. Therefore this test may be the optimal candidate to assess the behaviour of the method in the incompressible limit. We define a square computational domain of unit length and set wall boundary conditions everywhere. In particular, we fix a purely horizontal velocity at the top boundary $u_1 = 1$, $u_2 = 0$ and consider homogeneous no-slip boundary conditions on the bottom and lateral boundaries. As initial conditions, we consider a unit density, $\rho = 1$, the pressure $p = 10^4$ and an initial fluid at rest. The viscosity is set to $\mu = 10^{-2}$ so that $Re = 100$ and $M \approx 8 \cdot 10^{-3}$ are the characteristic Reynolds and Mach numbers of this test attending to the lid velocity. The artificial viscosity coefficient has been set to $c_\alpha = 2$. In the left plot of Figure 22, we show the Mach contour plot of the solution obtained with the LADER-ENO scheme overlapped by a sketch of the half dual elements employed. The right plot reports the comparison between the approximated and the reference solution for the horizontal and vertical velocities along the vertical and horizontal 1D cuts in the middle of the domain. An almost perfect match is observed.

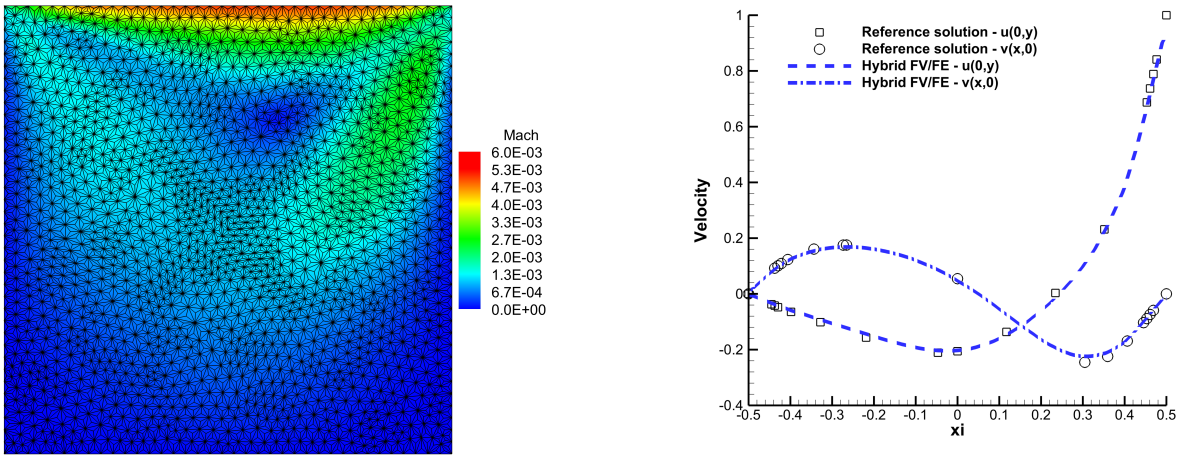

Figure 22: Solution of the lid-driven cavity test with $Re = 10^2$. In the left subfigure the dual half grid considered is depicted over the Mach number contour plot. The right plot shows the obtained 1D velocity cuts along $x = 0.5$ and $y = 0.5$ (blue dashed line) and the reference solution (black circles) given by [111].

4.8. Double shear layer

In this section we apply the new hybrid finite volume / finite element method for all Mach number flows developed in this paper to the well-known double shear layer problem, see e.g. [10, 64, 83]. The computational domain is given by $\Omega = [-1,1]^2$ and the initial condition reads

$$\rho^0(\mathbf{x}) = 1, \qquad u_1^0(\mathbf{x}) = \begin{cases} \tanh\left[\hat{\rho}(\hat{y} - \frac{1}{4})\right] & \text{if } \hat{y} \leq \frac{1}{2}, \\ \tanh\left[\hat{\rho}(\frac{3}{4} - \hat{y})\right] & \text{if } \hat{y} > \frac{1}{2}, \end{cases} \qquad u_2^0(\mathbf{x}) = \delta \sin(2\pi\hat{x}), \quad p^0(\mathbf{x}) = \frac{10^5}{\gamma}, \tag{87}$$

with the abbreviations $\hat{x} = \frac{x+1}{2}$ and $\hat{y} = \frac{y+1}{2}$. The remaining parameters of the setup of this test case are chosen as $\hat{\rho} = 30$, $\mu = 2 \cdot 10^{-4}$, $\lambda = 0$ and $\delta = 0.05$, see also [64, 83]. The characteristic Mach number of this test case is $M \approx 2 \cdot 10^{-3}$, hence we are again in the low Mach number regime. The domain is covered with 8192 primal elements and the boundary conditions are periodic everywhere. In Figure 23, we show contour plots of the vorticity at times $t \in \{0.8, 1.6, 2.4, 3.6\}$. Comparing our numerical solution with the one obtained in [71, 64] we note a very good agreement, although the scheme presented in this paper is only second order accurate, while in [71, 64] high order schemes have been employed.

4.9. Single Mach reflection problem

Let us now consider the single Mach reflection problem that can be found in [29] and for which experimental reference data are available in [29] and [112] under the form of Schlieren images. The test problem consists in a shock wave that is initially located in $x = -0.04$ and that travels to the right at a shock Mach number of $M = 1.7$, hitting a wedge that forms an angle of $\varphi = 25°$ with the x-axis. The pressure, p, and density, ρ, ahead of the shock are set to $\rho_0 = 1$ and $p_0 = 1/\gamma_g$, respectively, while for $x > -0.04$ we consider a fluid at rest. The post-shock values can be easily obtained from the Rankine-Hugoniot relations of the inviscid compressible Euler equations.

The computational domain is $\Omega = [0,3] \times [0,2]$, from which the 25° wedge is subtracted. It is discretized using 1237328 triangular elements of characteristic mesh spacing $h = 0.003$. For this test we set $c_\alpha = 1$. The pressure field obtained for a simulation run until $t_{\text{end}} = 1.2$ is depicted in Figure 24. The flow field obtained with the novel hybrid FV/FE scheme agrees well with the numerical and experimental reference solutions shown in [29]. The shock wave is properly resolved and located in the correct position at $x = 2$.

4.10. Shock-wedge interaction problem

In this section, we consider a flow that involves the interaction of a mild shock wave with a two-dimensional wedge, see also [113, 114]. Experimental reference data for this test are available in form of Schlieren photographs, see [112, 115]. The computational domain is given by $\Omega = [-2,6] \times [-3,3]$, excluding a wedge of length $L = 1$ and height $H = 1$ with its tip located in the origin. On all three edges of the wedge, we impose inviscid wall boundary conditions, while the upper and lower boundaries are periodic. On the left and on the right boundary, we impose the initial condition as Dirichlet boundary condition. The initial condition for a right-moving shock wave with shock Mach number $M_s = 1.3$, initially located in $x = -1$, is setup according to the Rankine-Hugoniot relations, see [113]. The pre-shock state (for $x > -1$) is given by $\rho_R = 1.4$, $\mathbf{u}_R = 0$, and $p_R = 1.0$. A triangular mesh with a characteristic mesh spacing of $h = 1/100$ is employed, leading to a total of 1080342 triangles. For this test, we set $c_\alpha = 0.5$. The pressure contours obtained with our hybrid FV/FE method are depicted in Figure 25 at several times. The location and shape of the shock and of the vortices shed behind the wedge compare qualitatively with those shown in [113, 114, 112, 115].

4.11. Supersonic flow at $M = 3$ over a circular blunt body

This last numerical test problem deals with the supersonic flow over a circular cylinder at Mach number $M = 3$. The computational domain is the part for which $x \leq 0$ of a circle of radius $R = 2$ centered in $\mathbf{x}_c = (0.5, 0)$, from which a circular blunt body of radius $r_b = 0.5$ centered in the origin is subtracted. The domain is discretized using a triangular mesh of characteristic mesh spacing $h = 1/200$ composed of 348964 triangles. For this test, we set $c_\alpha = 3$.

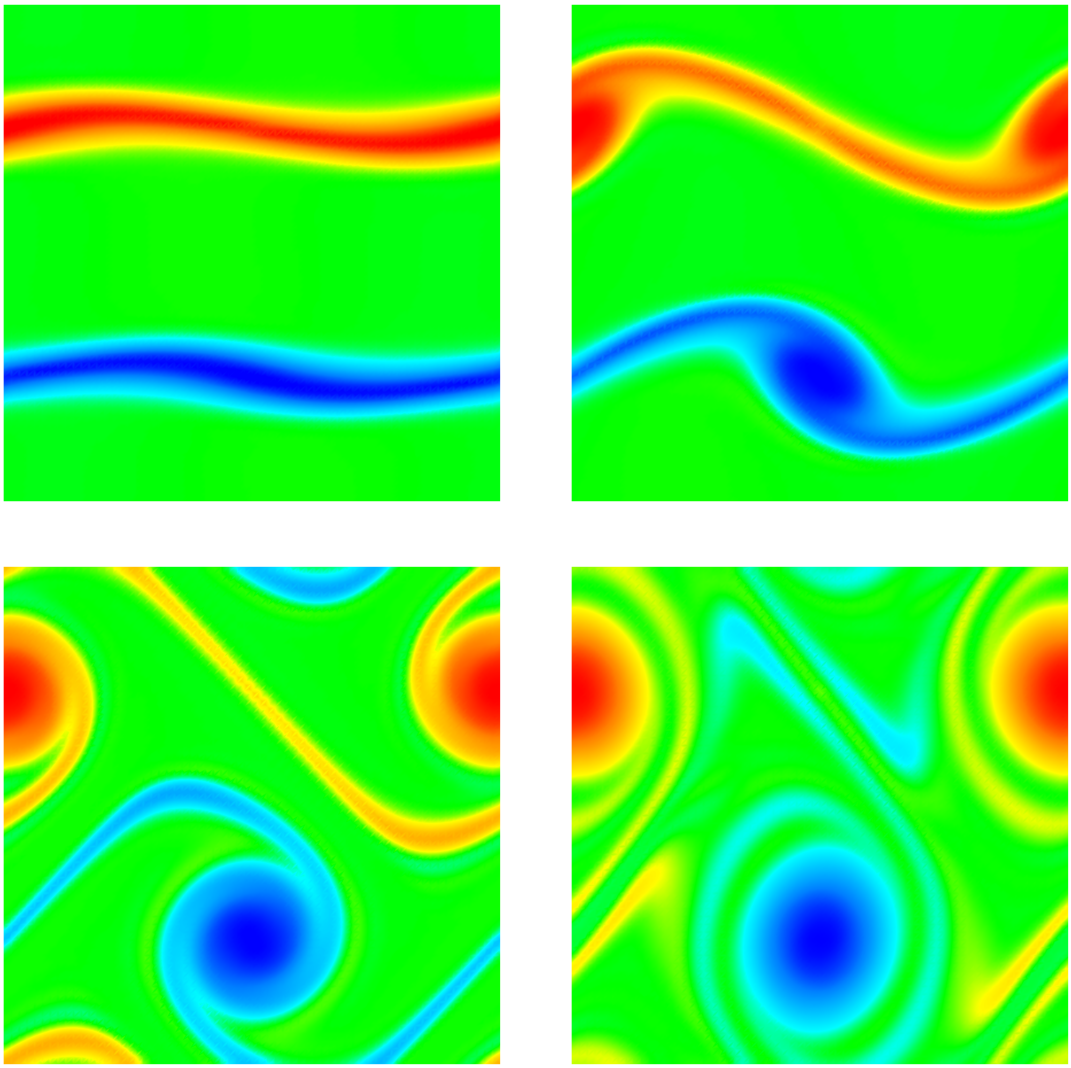

Figure 23: Contour plots of vorticity at times $t \in \{0.8, 1.6, 2.4, 3.6\}$ (from top left to bottom right) for the double shear layer test problem. The second order LADER scheme has been employed for the discretization of nonlinear convective terms.

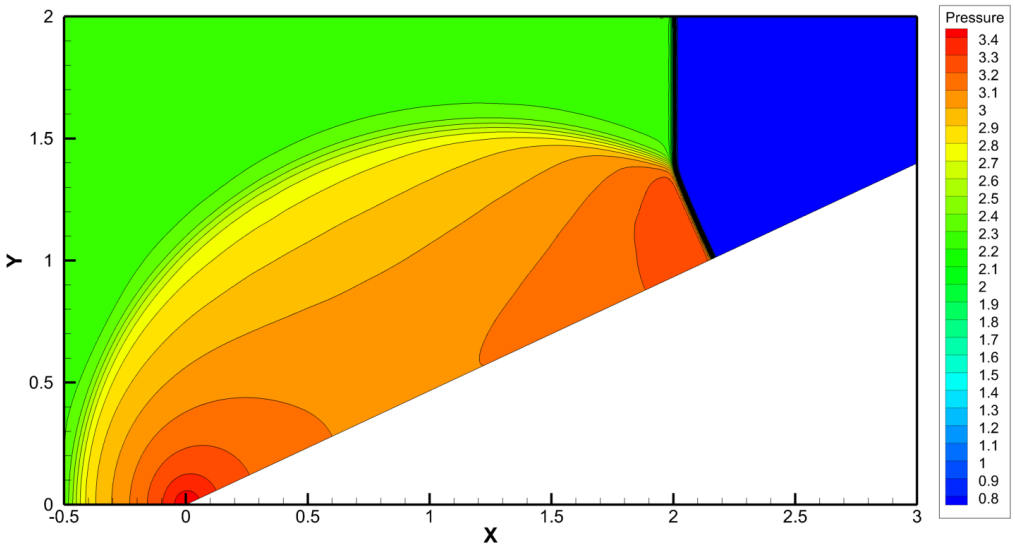

Figure 24: Pressure contours obtained at $t_{\text{end}} = 1.2$ for the single Mach reflection problem using the new all Mach number hybrid FV/FE scheme presented in this paper. The shock is in the correct location at $x = 2$.

The initial condition is $\rho = 1.4$, $\mathbf{u} = (3, 0)$, $p = 1$ in the entire computational domain. On the blunt body, inviscid wall boundary conditions are imposed. On the left inflow boundary, we impose the initial condition as Dirichlet boundary condition, while outflow is set on the right boundary. The computational results obtained with our hybrid FV/FE scheme are depicted in Figure 26 at time $t = 5$. The typical bow shock forms in front of the blunt body.

5. Conclusions

In this paper a novel asymptotic-preserving semi-implicit hybrid FV/FE algorithm has been proposed for the solution of all Mach number flows on staggered unstructured grids. The initial semi-discretization in time of Navier-Stokes equations allows a partial decoupling of the calculation of the linear momentum and of the density with respect to the solution of the pressure correction system. The first stage of the method involves the computation of the new density and an intermediate approximation of the linear momentum and total energy density, which account for the contribution of convection, diffusion, and gravity terms in the related conservative equations. Moreover, the pressure gradient at the previous time step is included so that the velocities would need only to be corrected with the pressure difference once it is computed. A local ADER methodology is employed to achieve a second order scheme in space and time, where we benefit from the dual mesh structure to approximate the gradients involved in the half in time reconstruction, hence reducing the stencil with respect to classical ADER methods. This procedure yields a good intermediate approximation of the linear momentum and total energy density to be provided for the computation of the pressure unknown on the projection stage. The splitting proposed following [36, 66] leads to an efficient numerical method in which the sound velocity is avoided on the eigenvalues computation of the transport-diffusion equations, approximated using an explicit scheme. Then, the pressure system is solved using classical implicit continuous finite element methods. Accordingly, the time step computed through the CFL condition is only limited by the flow velocity reducing the computational cost of the overall method. A key point of the proposed algorithm is the Picard iteration procedure that allows an iterative update of the linear momentum, enthalpy, and pressure variables avoiding the solution of a complex nonlinear system for the pressure. Once the pressure difference between two consecutive time steps is computed, the linear

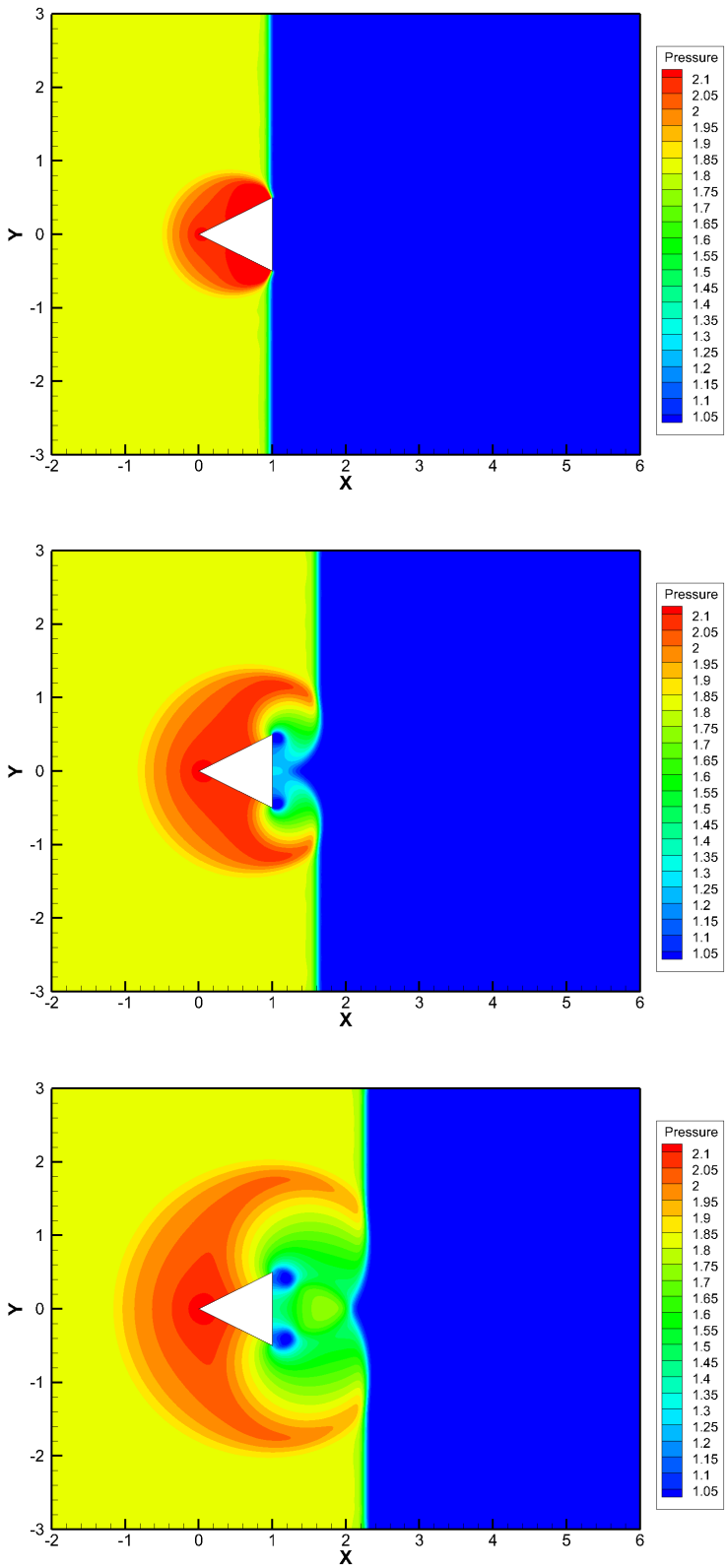

Figure 25: Shock-wedge interaction problem in 2D. Pressure contours using the hybrid FV/FE method on an unstructured triangular grid with mesh spacing $h = 1/100$. Output times from top to bottom: $t = 1.5$, $t = 2.0$, $t = 2.5$.

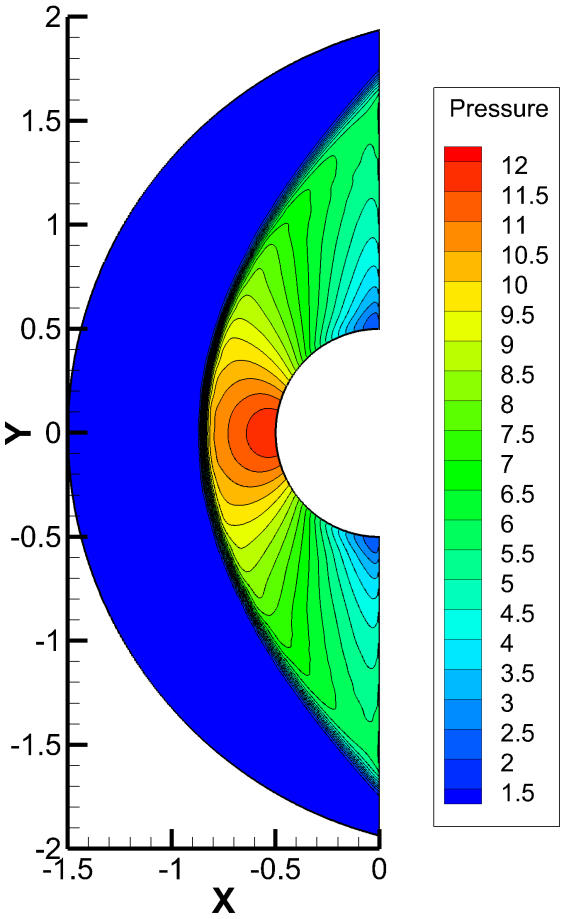

Figure 26: Pressure contours for the $M = 3$ flow over a circular blunt body at time $t = 5$.

momentum and energy are corrected. The proposed methodology has been carefully validated by comparison of the obtained results with available analytical and numerical solutions. The numerical tests ranging from the incompressible limit to supersonic flows show the capability of the method to address complex flow phenomena.

In the future, we plan to extend the hybrid FV-FE methodology in the context of shallow water equations making use of the seminal ideas presented in [12, 116, 117, 118, 119]. Moreover, more complex PDE systems, including natural involution constraints, like MHD equations, will be considered. To this end, the development of a structure-preserving scheme verifying the divergence-free condition will be essential, [120, 121, 122, 123, 124].

Acknowledgements

This work was financially supported by the Italian Ministry of Education, University and Research (MIUR) in the framework of the PRIN 2017 project *Innovative numerical methods for evolutionary partial differential equations and applications* and via the Departments of Excellence Initiative 2018–2022 attributed to DICAM of the University of Trento (grant L. 232/2016). Furthermore, LR and MEV have received funding

by Spanish MCIU under project MTM2017-86459-R and by FEDER and Xunta de Galicia funds under the ED431C 2017/60 project. SB was also funded by INdAM via a GNCS grant for young researchers and by a *UniTN starting grant* of the University of Trento. SB, LR and MD are members of the GNCS group of INdAM.

References

[1] S. Busto, J. L. Ferrín, E. F. Toro, M. E. Vázquez-Cendón, A projection hybrid high order finite volume/finite element method for incompressible turbulent flows, J. Comput. Phys. 353 (2018) 169–192.
[2] S. Klainermann, A. Majda, Singular limits of quasilinear hyperbolic systems with large parameters and the incompressible limit of compressible fluid, Comm. Pure Appl. Math. 34 (1981) 481–524.
[3] S. Klainermann, A. Majda, Compressible and incompressible fluids, Communications on Pure and Applied Mathematics 35 (1982) 629–651.
[4] F. Harlow, J. Welch, Numerical calculation of time-dependent viscous incompressible flow of fluid with a free surface, Phys. Fluids 8 (1965) 2182–2189.
[5] A. Chorin, A numerical method for solving incompressible viscous flow problems, J. Comput. Phys. 2 (1967) 12–26.
[6] A. Chorin, Numerical solution of the Navier–Stokes equations, Math. Comput. 23 (1968) 341–354.
[7] S. V. Patankar, D. B. Spalding, A calculation procedure for heat, mass and momentum transfer in three-dimensional parabolic flows, Int J Heat Mass Transfer 15 (10) (1972) 1787–1806.
[8] V. Patankar, Numerical Heat Transfer and Fluid Flow, Hemisphere Publishing Corporation, 1980.
[9] J. van Kan, A second-order accurate pressure correction method for viscous incompressible flow, SIAM Journal on Scientific and Statistical Computing 7 (1986) 870–891.
[10] J. B. Bell, P. Colella, H. M. Glaz, A second-order projection method for the incompressible Navier-Stokes equations, J. Comput. Phys. 85 (2) (1989) 257–283.
[11] C. W. Hirt, B. D. Nichols, Volume of fluid (VOF) method for dynamics of free boundaries, J. Comput. Phys. 39 (1981) 201–225.
[12] V. Casulli, A semi–implicit numerical method for the free–surface Navier–Stokes equations, International Journal for Numerical Methods in Fluids 74 (2014) 605–622.
[13] C. Taylor, P. Hood, A numerical solution of the Navier-Stokes equations using the finite element technique, Computers and Fluids 1 (1973) 73–100.
[14] A. Brooks, T. Hughes, Stream-line upwind/Petrov Galerkin formulstion for convection dominated flows with particular emphasis on the incompressible Navier-Stokes equation, Computer Methods in Applied Mechanics and Engineering 32 (1982) 199–259.
[15] T. Hughes, M. Mallet, M. Mizukami, A new finite element formulation for computational fluid dynamics: II. Beyond SUPG, Computer Methods in Applied Mechanics and Engineering 54 (1986) 341–355.
[16] M. Fortin, Old and new finite elements for incompressible flows, International Journal for Numerical Methods in Fluids 1 (1981) 347–364.
[17] R. Verfürth, Finite element approximation of incompressible Navier-Stokes equations with slip boundary condition II, Numerische Mathematik 59 (1991) 615–636.
[18] J. G. Heywood, R. Rannacher, Finite element approximation of the nonstationary Navier-Stokes Problem. I. Regularity of solutions and second order error estimates for spatial discretization, SIAM J. Numer. Anal. 19 (1982) 275–311.
[19] J. G. Heywood, R. Rannacher, Finite element approximation of the nonstationary Navier-Stokes Problem. III. Smoothing property and higher order error estimates for spatial discretization, SIAM J. Numer. Anal. 25 (1988) 489–512.
[20] P. Lax, B. Wendroff, Systems of conservation laws, Commun. Pur. Appl. Math. 13 (2) (1960) 217–237.
[21] S. K. Godunov, A finite difference method for the computation of discontinuous solutions of the equations of fluid dynamics, Mat. Sb. 47 (1959) 357–393.
[22] P. Roe, Approximate Riemann solvers, parameter vectors, and difference schemes, J. Comput. Phys. 43 (1981) 357–372.
[23] S. Osher, F. Solomon, Upwind difference schemes for hyperbolic conservation laws, Math. Comput. 38 (1982) 339–374.
[24] A. Harten, P. Lax, B. van Leer, On upstream differencing and Godunov-type schemes for hyperbolic conservation laws, Vol. 25, 1983, pp. 35–61.
[25] B. Einfeldt, C. Munz, P. Roe, B. Sjögreen, On Godunov-type methods near low densities, J. Comput. Phys. 92 (1991) 273–295.
[26] C. D. Munz, On Godunov–type schemes for Lagrangian gas dynamics, SIAM Journal on Numerical Analysis 31 (1994) 17–42.
[27] E. F. Toro, M. Spruce, W. Speares, Restoration of the contact surface in the Harten-Lax-van Leer Riemann solver, Journal of Shock Waves 4 (1994) 25–34.
[28] R. J. LeVeque, Finite Volume Methods for Hyperbolic Problems, Cambridge Texts in Applied Mathematics, 2002.
[29] E. F. Toro, Riemann solvers and numerical methods for fluid dynamics: A practical introduction, Springer, 2009.
[30] V. Casulli, D. Greenspan, Pressure method for the numerical solution of transient, compressible fluid flows, Int. J. Numer. Methods Fluids 4 (1984) 1001–1012.
[31] A. Meister, Asymptotic single and multiple scale expansions in the low mach number limit, SIAM Journal on Applied Mathematics 60 (1) (1999) 256–271.
[32] C. Munz, R. Klein, S. Roller, K. Geratz, The extension of incompressible flow solvers to the weakly compressible regime, Computers and Fluids 32 (2003) 173–196.

[33] R. Klein, Semi-implicit extension of a godunov-type scheme based on low mach number asymptotics I: one-dimensional flow, J. Comput. Phys. 121 (1995) 213–237.

[34] R. Klein, N. Botta, T. Schneider, C. Munz, S.Roller, A. Meister, L. Hoffmann, T. Sonar, Asymptotic adaptive methods for multi-scale problems in fluid mechanics, Journal of Engineering Mathematics 39 (2001) 261–343.

[35] J. Park, C. Munz, Multiple pressure variables methods for fluid flow at all Mach numbers, International journal for numerical methods in fluids 49 (8) (2005) 905–931.

[36] E. Toro, M. Vázquez-Cendón, Flux splitting schemes for the Euler equations, Computers and Fluids 70 (2012) 1–12.

[37] F. Cordier, P. Degond, A. Kumbaro, An Asymptotic-Preserving all-speed scheme for the Euler and Navier-Stokes equations, J. Comput. Phys. 231 (2012) 5685–5704.

[38] P. Degond, M. Tang, All speed scheme for the low Mach number limit of the isentropic Euler equations, Comm. Comput. Phys. 10 (1) (2011) 1–31.

[39] M. Dumbser, V. Casulli, A conservative, weakly nonlinear semi-implicit finite volume scheme for the compressible Navier-Stokes equations with general equation of state, Applied Mathematics and Computation 272 (2016) 479–497.

[40] S. Boscarino, G. Russo, L. Scandurra, All Mach number second order semi-implicit scheme for the Euler equations of gasdynamics, J. Sci. Comput. 77 (2018) 850–884.

[41] G. Dimarco, R. Loubère, V. Michel-Dansac, M. Vignal, Second-order implicit-explicit total variation diminishing schemes for the euler system in the low mach regime, J. Comput. Phys. 372 (2018) 178 – 201.

[42] E. Abbate, A. Iollo, G. Puppo, An asymptotic-preserving all-speed scheme for fluid dynamics and nonlinear elasticity, SIAM Journal on Scientific Computing 41 (2019) A2850–A2879.

[43] S. Avgerinos, F. Bernard, A. Iollo, G. Russo, Linearly implicit all mach number shock capturing schemes for the euler equations, J. Comput. Phys. 393 (2019) 278 – 312.

[44] W. Boscheri, G. Dimarco, R. Loubère, M. Tavelli, M. Vignal, A second order all mach number imex finite volume solver for the three dimensional euler equations, Journal of Computational Physics 415 (2020) 109486.

[45] W. Boscheri, G. Dimarco, M. Tavelli, An efficient second order all Mach finite volume solver for the compressible Navier–Stokes equations, Computer Methods in Applied Mechanics and Engineering 374 (2021) 113602.

[46] W. Boscheri, L. Pareschi, High order pressure-based semi-implicit IMEX schemes for the 3D Navier-Stokes equations at all Mach numbers, Journal of Computational PhysicsTo appear (2021).

[47] S. Shanmuganathan, D. L. Youngs, J. Griffond, B. Thornber, R. Williams, Accuracy of high-order density-based compressible methods in low mach vortical flows, International Journal for Numerical Methods in Fluids 74 (2014) 335–358.

[48] N. Fleischmann, S. Adami, X. Hu, N. Adams, A low dissipation method to cure the grid-aligned shock instability, Journal of Computational Physics 401 (2020) 109004.

[49] F. Bassi, S. Rebay, A high-order accurate discontinuous finite element method for the numerical solution of the compressible Navier-Stokes equations, J. Comput. Phys. 131 (1997) 267–279.

[50] C. Baumann, J. Oden, A discontinuous hp finite element method for convection-diffusion problems, Comput. Methods Appl. Mech. Eng. 175 (3-4) (1999) 311–341.

[51] C. Baumann, J. Oden, A discontinuous hp finite element method for the euler and navier-stokes equations, Int. J. Numer. Methods Fluids 31 (1) (1999) 79–95.

[52] B. Cockburn, C. W. Shu, The local discontinuous Galerkin method for time-dependent convection diffusion systems, SIAM Journal on Numerical Analysis 35 (1998) 2440–2463.

[53] B. Cockburn, C. W. Shu, Runge-Kutta discontinuous Galerkin methods for convection-dominated problems, J. Sci. Comput. 16 (2001) 199–224.

[54] F. Bassi, A. Crivellini, D. D. Pietro, S. Rebay, An implicit high-order discontinuous Galerkin method for steady and unsteady incompressible flows, Computers and Fluids 36 (2007) 1529–1546.

[55] E. Ferrer, R. Willden, A high order discontinuous galerkin finite element solver for the incompressible navier–stokes equations, Computer and Fluids 46 (2011) 224–230.

[56] N. Nguyen, J. Peraire, B. Cockburn, An implicit high-order hybridizable discontinuous galerkin method for the incompressible navier-stokes equations, J. Comput. Phys. 230 (2011) 1147–1170.

[57] S. Rhebergen, B. Cockburn, A space-time hybridizable discontinuous Galerkin method for incompressible flows on deforming domains, J. Comput. Phys. 231 (2012) 4185–4204.

[58] S. Rhebergen, B. Cockburn, J. J. van der Vegt, A space-time discontinuous Galerkin method for the incompressible Navier-Stokes equations, J. Comput. Phys. 233 (2013) 339–358.

[59] A. Crivellini, V. D'Alessandro, F. Bassi, High-order discontinuous Galerkin solutions of three-dimensional incompressible RANS equations, Computers and Fluids 81 (2013) 122–133.

[60] B. Klein, F. Kummer, M. Oberlack, A SIMPLE based discontinuous Galerkin solver for steady incompressible flows, J. Comput. Phys. 237 (2013) 235–250.

[61] V. Dolejsi, Semi-implicit interior penalty discontinuous Galerkin methods for viscous compressible flows, Comm. Comput. Phys. 4 (2008) 231–274.

[62] V. Dolejsi, M. Feistauer, A semi-implicit discontinuous Galerkin finite element method for the numerical solution of inviscid compressible flow, J. Comput. Phys. 198 (2004) 727–746.

[63] V. Dolejsi, M. Feistauer, J. Hozman, Analysis of semi-implicit DGFEM for nonlinear convection-diffusion problems on nonconforming meshes, Comput. Methods Appl. Mech. Eng. 196 (2007) 2813–2827.

[64] M. Tavelli, M. Dumbser, A staggered space-time discontinuous Galerkin method for the incompressible Navier-Stokes equations on two-dimensional triangular meshes, Comput. Fluids 119 (2015) 235 – 249.

[65] M. Tavelli, M. Dumbser, A staggered space-time discontinuous Galerkin method for the three-dimensional incompressible Navier-Stokes equations on unstructured tetrahedral meshes, J. Comput. Phys. 319 (2016) 294 – 323.

[66] M. Tavelli, M. Dumbser, A pressure-based semi-implicit space-time discontinuous Galerkin method on staggered unstructured meshes for the solution of the compressible Navier-Stokes equations at all Mach numbers, J. Comput. Phys. 341 (2017) 341 – 376.

[67] F. Fambri, M. Dumbser, Spectral semi-implicit and space-time discontinuous Galerkin methods for the incompressible Navier-Stokes equations on staggered Cartesian grids, Applied Numerical Mathematics 110 (2016) 41–74.

[68] F. Fambri, M. Dumbser, Semi-implicit discontinuous Galerkin methods for the incompressible Navier-Stokes equations on adaptive staggered Cartesian grids, Computer Methods in Applied Mechanics and Engineering 324 (2017) 170–203.

[69] S. Busto, M. Tavelli, W. Boscheri, M. Dumbser, Efficient high order accurate staggered semi-implicit discontinuous galerkin methods for natural convection problems, Comput. Fluids 198 (2020) 104399.

[70] I. Peshkov, E. Romenski, A hyperbolic model for viscous Newtonian flows, Continuum Mechanics and Thermodynamics 28 (2016) 85–104.

[71] M. Dumbser, I. Peshkov, E. Romenski, O. Zanotti, High order ADER schemes for a unified first order hyperbolic formulation of continuum mechanics: Viscous heat-conducting fluids and elastic solids, J. Comput. Phys. 314 (2016) 824 – 862.

[72] S. Busto, S. Chiocchetti, M. Dumbser, E. Gaburro, I. Peshkov, High order ADER schemes for continuum mechanics, Frontiers in Physiccs 8 (2020) 32. doi:10.3389/fphy.2020.00032.

[73] W. Boscheri, M. Dumbser, M. Ioriatti, I. Peshkov, E. Romenski, A structure-preserving staggered semi-implicit finite volume scheme for continuum mechanics, Journal of Computational Physics 2021 (2010) 109866.

[74] I. Peshkov, M. Dumbser, W. Boscheri, E. Romenski, S. Chiocchetti, M. Ioriatti, Modeling solid-fluid transformation in non-newtonian viscoplastic flows with a unified flow theory, Computers and FluidsSubmitted.

[75] S. Godunov, An interesting class of quasilinear systems, Dokl. Akad. Nauk SSSR 139(3) (1961) 521–523.

[76] S. Godunov, E. Romenski, Nonstationary equations of the nonlinear theory of elasticity in Euler coordinates., Journal of Applied Mechanics and Technical Physics 13 (1972) 868–885.

[77] S. Godunov, Symmetric form of the magnetohydrodynamic equation, Numerical Methods for Mechanics of Continuum Medium 3 (1) (1972) 26–34.

[78] E. Romenski, Hyperbolic systems of thermodynamically compatible conservation laws in continuum mechanics, Mathematical and computer modelling 28(10) (1998) 115–130.

[79] S. Godunov, E. Romenski, Elements of Continuum Mechanics and Conservation Laws, Kluwer Academic/ Plenum Publishers, 2003.

[80] L. Li, J. Luo, H. Nishikawa, H. Luo, Reconstructed discontinuous Galerkin methods for compressible flows based on a new hyperbolic navier-stokes system, Journal of Computational Physics (2021) 110058.

[81] A. Bermúdez, J. L. Ferrín, L. Saavedra, M. E. Vázquez-Cendón, A projection hybrid finite volume/element method for low-Mach number flows, J. Comp. Phys. 271 (2014) 360–378.

[82] S. Busto, G. Stabile, G. Rozza, M. Vázquez-Cendón, POD-Galerkin reduced order methods for combined Navier-Stokes transport equations based on a hybrid FV-FE solver, Computers & Mathematics with Applications 79 (2) (2020) 256 – 273.

[83] A. Bermúdez, S. Busto, M. Dumbser, J. Ferrín, L. Saavedra, M. Vázquez-Cendón, A staggered semi-implicit hybrid fv/fe projection method for weakly compressible flows, Journal of Computational Physics 421 (2020) 109743.

[84] S. Busto, E. F. Toro, M. E. Vázquez-Cendón, Design and analisis of ADER–type schemes for model advection–diffusion–reaction equations, J. Comp. Phys. 327 (2016) 553–575.

[85] A. Bermúdez, S. Busto, J. L. Ferrín, L. Saavedra, E. F. Toro, M. E. Vázquez-Cendón, SEMA SIMAI Springer Series. Computational Mathematics, Numerical Analysis and Applications, Springer, 2017, Ch. A projection hybrid finite volume-ADER/finite element method for turbulent Navier-Stokes, pp. 201–206.

[86] A. Bermúdez, S. Busto, M. Dumbser, F. Ferrín, V.-C. M. Saavedra, L., A staggered semi-implicit hybrid FV/FE projection method for weakly compressible flows, J. Comput. Phys. 421 (2020) 109743.

[87] L. Brugnano, V. Casulli, Iterative solution of piecewise linear systems, SIAM Journal on Scientific Computing 30 (2007) 463–472.

[88] L. Brugnano, V. Casulli, Iterative solution of piecewise linear systems and applications to flows in porous media, SIAM Journal on Scientific Computing 31 (2009) 1858–1873.

[89] L. Brugnano, A. Sestini, Iterative solution of piecewise linear systems for the numerical solution of obstacle problems, Journal of Numerical Analysis, Industrial and Applied Mathematics 6 (2012) 67–82.

[90] V. Casulli, P. Zanolli, A nested Newton–type algorithm for finite volume methods solving Richards' equation in mixed form, SIAM Journal on Scientific Computing 32 (2009) 2255–2273.

[91] V. Casulli, P. Zanolli, Iterative solutions of mildly nonlinear systems, Journal of Computational and Applied Mathematics 236 (2012) 3937–3947.

[92] V. V. Rusanov, The calculation of the interaction of non-stationary shock waves and obstacles, USSR Computational Mathematics and Mathematical Physics 1 (1962) 304–320.

[93] S. Busto, Contributions to the numerical solution of heterogeneous fluid mechanics models, Ph.D. thesis, Universidade de Santiago de Compostela (2018).

[94] E. F. Toro, R. C. Millington, L. A. M. Nejad, Godunov methods, Springer, 2001, Ch. Towards very high order Godunov schemes.

[95] R. Millington, E. Toro, L. Nejad, Arbitrary high order methods for conservation laws i: The one dimensional scalar case, Ph.D. thesis, Manchester Metropolitan University, Department of Computing and Mathematics (June 1999).

[96] M. Dumbser, C. Enaux, E. F. Toro, Finite volume schemes of very high order of accuracy for stiff hyperbolic balance laws, J. Comput. Phys. 227 (8) (2008) 3971 – 4001.

[97] W. Boscheri, M. Dumbser, A direct arbitrary-lagrangian-eulerian ADER-WENO finite volume scheme on unstructured tetrahedral meshes for conservative and non-conservative hyperbolic systems in 3D, J. Comput. Phys. 275 (2014) 484–523.

[98] T. Barth, D. Jespersen, The design and application of upwind schemes on unstructured meshes, Tech. rep. (1989).

[99] P. L. Roe, Modelling of Discontinuous Flows, Vol. 22, 1985.

[100] S. Clain, S. Diot, R. Loubère, A high-order finite volume method for systems of conservation lawsmulti-dimensional optimal order detection (mood), J. Comput. Phys. 230 (2011) 4028–4050.

[101] V. Casulli, P. Zanolli, A nested newton-type algorithm for finite volume methods solving richards' equation in mixed form, SIAM J. Sci. Comput. 32 (4) (2010) 2255–2273.

[102] M. Dumbser, D. S. Balsara, E. F. Toro, C.-D. Munz, A unified framework for the construction of one-step finite volume and discontinuous Galerkin schemes on unstructured meshes, J. Comput. Phys. 227 (18) (2008) 8209–8253.

[103] L. Pareschi, G. Russo, Implicit-explicit Runge-Kutta schemes for stiff systems of differential equations, Advances in the Theory of Computational Mathematics 3 (2000) 269–288.

[104] G. A. Sod, A survey of several finite difference methods for systems of nonlinear hyperbolic conservation laws, J. Comput. Phys. 27 (1) (1978) 1 – 31.

[105] P. Woodward, P. Colella, The numerical simulation of two-dimensional fluid flow with strong shocks, Journal of Computational Physics 54 (1984) 115–173.

[106] V. A. Titarev, E. F. Toro, ADER schemes for three-dimensional non-linear hyperbolic systems, J. Comp. Phys. 204 (2) (2005) 715–736.

[107] H. Schlichting, K. Gersten, Boundary-layer theory, Springer, 2016.

[108] R. Becker, Stosswelle und Detonation, Physik 8 (1923) 321.

[109] A. Bonnet, J. Luneau, Aérodynamique. Théories de la dynamique des fluides, Cepadues Editions, Toulouse, 1989, iSBN: 2.85428.218.3.

[110] M. Dumbser, I. Peshkov, E. Romenski, O. Zanotti, High order ADER schemes for a unified first order hyperbolic formulation of continuum mechanics: Viscous heat-conducting fluids and elastic solids, Journal of Computational Physics 314 (2016) 824–862.

[111] U. Ghia, K. Ghia, C. Shin, High-re solutions for incompressible flow using the Navier-Stokes equations and a multigrid method, J. Comput. Phys. 48 (3) (1982) 387 – 411.

[112] M. van Dyke, An album of fluid motion, The Parabolic Press, 2005.

[113] M. Dumbser, M. Käser, V. A. Titarev, E. F. Toro, Quadrature-free non-oscillatory finite volume schemes on unstructured meshes for nonlinear hyperbolic systems, Journal of Computational Physics 226 (2007) 204–243.

[114] F. Kemm, E. Gaburro, F. Thein, M. Dumbser, A simple diffuse interface approach for compressible flows around moving solids of arbitrary shape based on a reduced Baer-Nunziato model, Computers and Fluids 204 (2020) 104536.

[115] H. Schardin, in: Proc. VII Int. Cong. High Speed Photg., Darmstadt, O. Helwich Verlag, 1965, pp. 113–119.

[116] V. Casulli, R. T. Cheng, Semi-implicit finite difference methods for three–dimensional shallow water flow, International Journal for Numerical Methods in Fluids 15 (1992) 629–648.

[117] V. Casulli, R. A. Walters, An unstructured grid, three–dimensional model based on the shallow water equations, International Journal for Numerical Methods in Fluids 32 (2000) 331–348.

[118] S. C. Kramer, G. S. Stelling, A conservative unstructured scheme for rapidly varied flows, International Journal for Numerical Methods in Fluids 58 (2008) 183–212.

[119] M. Tavelli, M. Dumbser, A high order semi-implicit discontinuous Galerkin method for the two dimensional shallow water equations on staggered unstructured meshes, Appl. Math. Comput. 234 (2014) 623–644.

[120] P. K.G., Upwind and High-Resolution Schemes, Springer, 1997, Ch. An Approximate Riemann Solver for Magnetohydrodynamics.

[121] C. Munz, P. Omnes, R. Schneider, E. Sonnendrücker, U. Voss, Divergence correction techniques for Maxwell solvers based on a hyperbolic model, Journal of Computational Physics 161 (2000) 484–511.

[122] D. Balsara, Second order accurate schemes for magnetohydrodynamics with divergence-free reconstruction, The Astrophysical Journal Supplement Series 151 (08 2003). doi:10.1086/381377.

[123] D. Balsara, M. Dumbser, R. Abgrall, Multidimensional HLL and HLLC Riemann solvers for unstructured meshes-with application to Euler and MHD flows, Journal of Computational Physics 261 (2014) 172–208.

[124] M. Dumbser, D. Balsara, M. Tavelli, F. Fambri, A divergence-free semi-implicit finite volume scheme for ideal, viscous, and resistive magnetohydrodynamics, International Journal for Numerical Methods in Fluids 89 (1-2) (2019) 16–42.